





# Inertial focusing of spherical capsule in pulsatile channel flows

Naoki Takeishi<sup>1</sup> , Kenta Ishimoto<sup>2</sup> , Naoto Yokoyama<sup>3</sup>  and Marco Edoardo Rosti<sup>4</sup> 

<sup>1</sup>Department of Mechanical Engineering, Faculty of Engineering, Kyushu University, 744 Motooka Nishi-ku, Fukuoka 819-0395, Japan

<sup>2</sup>Research Institute for Mathematical Sciences, Kyoto University, Kitashirakawa Oiwake-cho, Sakyo-ku, Kyoto 606-8502, Japan

<sup>3</sup>Department of Mechanical Engineering, Tokyo Denki University, 5 Senju-Asahi, Adachi, Tokyo 120-8551, Japan

<sup>4</sup>Complex Fluids and Flows Unit, Okinawa Institute of Science and Technology Graduate University, 1919-1 Tancha, Onna-son, Okinawa 904-0495, Japan

**Corresponding author:** Naoki Takeishi, [takeishi.naoki.008@m.kyushu-u.ac.jp](mailto:takeishi.naoki.008@m.kyushu-u.ac.jp)

(Received 3 September 2024; revised 18 December 2024; accepted 11 February 2025)

We present numerical analysis of the lateral movement of a spherical capsule in the steady and pulsatile channel flow of a Newtonian fluid for a wide range of oscillatory frequencies. Each capsule membrane satisfying strain-hardening characteristics is simulated for different Reynolds numbers  $Re$  and capillary numbers  $Ca$ . Our numerical results showed that capsules with high  $Ca$  exhibit axial focusing at finite  $Re$  similarly to the inertialess case. We observe that the speed of the axial focusing can be substantially accelerated by making the driving pressure gradient oscillate in time. We also confirm the existence of an optimal frequency that maximises the speed of axial focusing, which remains the same found in the absence of inertia. For relatively low  $Ca$ , however, the capsule exhibits off-centre focusing, resulting in various equilibrium radial positions depending on  $Re$ . Our numerical results further clarify the existence of a specific  $Re$  for which the effect of the flow pulsation to the equilibrium radial position is maximum. The roles of channel size on the lateral movements of the capsule are also addressed. Throughout our analyses, we have quantified the radial position of the capsule in a tube based on an empirical expression. Given that the speed of inertial focusing can be controlled by the oscillatory frequency, the results obtained here can be used for label-free cell alignment/sorting/separation techniques, e.g. for circulating tumour cells in cancer patients or precious haematopoietic cells such as colony-forming cells.



Downloaded from <https://www.cambridge.org/core>. IP address: 3.15.226.150, on 17 Apr 2025 at 05:03:13, subject to the Cambridge Core terms of use, available at <https://www.cambridge.org/core/terms>. <https://doi.org/10.1017/jfm.2025.184>

**Key words:** capsule/cell dynamics, membranes, microfluidics

## 1. Introduction

In a pipe flow at a finite channel (or particle) Reynolds number  $Re$  ( $Re_p$ ), a rigid spherical particle exhibits migration perpendicular to the flow direction, originally reported by Segre & Silberberg (1962), the so-called inertial focusing or tubular pinch effect, where the particles equilibrate at a distance from the channel centreline as a consequence of the force balance between the shear-induced and wall-induced lift forces. The phenomenon is of fundamental importance in microfluidic techniques such as label-free cell alignment, sorting and separation techniques (Martel & Toner 2014; Warkiani *et al.* 2016; Zhou *et al.* 2019). Although the techniques allow us to reduce the complexity and cost of clinical applications by using small amounts of blood samples, archetypal inertial focusing system requires steady laminar flow through long channel distances  $L_f$ , which can be estimated as  $L_f = \pi \mathcal{H}/(Re_p f_l)$ , where  $\mathcal{H}$  is the dimension of the channel (or its hydraulic diameter) and  $f_l$  is a non-dimensional lift coefficient (Di Carlo 2009). So far, various kinds of geometries have been proposed to achieve the required distance for inertial focusing in a compact space, e.g. sinusoidal, spiral and hybrid channels (Bazaz *et al.* 2020). Without increasing  $Re_p$ , the recent experimental study by Mutlu *et al.* (2018) achieved inertial focusing of  $0.5 \mu\text{m}$  particles ( $Re_p \approx 0.005$ ) in short channels by using oscillatory channel flows. Since the oscillatory flows allow a suspended particle to increase its total travel distance without net displacement along the flow direction, using oscillatory flow can be an alternative and practical strategy for inertial focusing in microfluidic devices. Recently, Vishwanathan & Juarez (2021) experimentally investigated the effects of the Womersley number ( $\alpha$ ) on inertial focusing in planar pulsatile flows, and evaluated the lateral migration (or off-centre focusing) speed on a small and weakly inertial particle for different oscillatory frequencies. They concluded that inertial focusing is achieved in only a fraction of the channel length (1%–10%) compared with what would be required in a steady flow (Vishwanathan & Juarez 2021). Sun *et al.* (2009) performed two-dimensional (2-D) simulations of a neutrally buoyant circular particle in oscillatory pressure-driven channel flows for  $Re \geq 50$ . Their results indicated that lower oscillatory frequency makes the equilibrium position closer to the channel centreline, while higher oscillatory frequency maintains the equilibrium positions similarly to the steady flow conditions. However, it remains unknown whether the equilibrium position of deformable capsules under pulsatile channel flows can be formulated in the same context as that of a rigid circular particle.

While a number of studies have analysed the off-centre focusing of rigid spherical particles under steady flow by a variety of approaches, such as analytical calculations (Ho & Leal 1974; Schonberg & Hinch 1989; Asmolov 1999), numerical simulations (Bazaz *et al.* 2020; Feng *et al.* 1994; Shao *et al.* 2008; Yang *et al.* 2005; Yu *et al.* 2004) and experimental observations (Di Carlo 2009; Karnis *et al.* 1966; Matas *et al.* 2004), the inertial focusing of deformable particles such as biological cells, consisting of an internal fluid enclosed by a thin membrane, has not yet been fully described, especially under unsteady flows. Due to their deformability, the problem of inertial focusing of deformable particles is more complex than with rigid spherical particles, as originally reported by Segre & Silberberg (1962). It is now well known that a deformable particle at low  $Re$  migrates towards the channel axis under steady laminar flow (Karnis *et al.* 1963). Hereafter, we call this phenomenon ‘axial focusing’. A recent numerical study showed that, in almost inertialess condition, the axial focusing of a deformable spherical capsule

can be accelerated by the flow pulsation at a specific frequency (Takeishi & Rosti 2023). For finite  $Re$  ( $>1$ ), however, it is still uncertain whether the flow pulsation can enhance the off-centre focusing or impede it (i.e. axial focusing). Therefore, the primary objective of this study is to clarify whether a capsule lateral movement at finite  $Re$  in a pulsatile channel flow can be altered by its deformability. The second objective is to clarify whether the  $Re$ -dependent equilibrium radial position of a capsule in a channel or travelling time are controllable by oscillatory frequency.

At least for steady channel flows, inertial focusing of deformable capsules including biological cells have been investigated in recent years both by means of experimental observations (Warkiani *et al.* 2016; Zhou *et al.* 2019) and numerical simulations (Raffiee *et al.* 2017; Schaaf & Stark 2017; Takeishi *et al.* 2022). For instance, Hur *et al.* (2011) experimentally investigated the inertial focusing of various cell types (including red blood cells, leukocytes and cancer cells such as a cervical carcinoma cell line, breast carcinoma cell line and osteosarcoma cell line) with a cell-to-channel size ratio  $0.1 \leq d_0/W \leq 0.8$ , using a rectangular channel with a high aspect ratio of  $W/H \approx 0.5$ , where  $d_0$ ,  $W$  and  $H$  are the cell equilibrium diameter, channel width and height, respectively. They showed that the cells can be separated according to their size and deformability (Hur *et al.* 2011). The experimental results can be qualitatively described using a spherical capsule (Kilimnik *et al.* 2011) or droplet model (Chen *et al.* 2014). In more recent experiments by Hadikhani *et al.* (2018), the authors investigated the effect of  $Re$  ( $1 < Re < 40$ ) and capillary number  $Ca$  – ratio between the fluid viscous force and the membrane elastic force – ( $0.1 < Ca < 1$ ) on the lateral equilibrium of bubbles in rectangular microchannels and different bubble-to-channel size ratios with  $0.48 \leq d_0/W \leq 0.84$ . The equilibrium position of such soft particles results from the competition between  $Re$  and  $Ca$ , because high  $Re$  induces off-centre focusing, while high  $Ca$ , i.e. high deformability, allows axial focusing. However, notwithstanding these recent advancements, a comprehensive understanding of the effect on the inertial focusing of these two fundamental parameters has not been fully established yet.

Numerical analysis more clearly showed that the ‘deformation-induced lift force’ becomes stronger as the particle deformation is increased (Raffiee *et al.* 2017; Schaaf & Stark 2017). Although a number of numerical analyses regarding inertial focusing have been reported in recent years mostly for spherical particles (Bazaz *et al.* 2020; Banerjee *et al.* 2021), the equilibrium positions of soft particles is still debated owing to the complexity of the phenomenon. Kilimnik *et al.* (2011) showed that the equilibrium position in a cross-section of a rectangular microchannel with  $d_0/H = 0.2$  shifts towards the wall as  $Re$  increases from 1 to 100. Schaaf & Stark (2017) also performed numerical simulations of spherical capsules in a square channel for  $0.1 \leq d_0/H \leq 0.4$  and  $5 \leq Re \leq 100$  without viscosity contrast, and showed that the equilibrium position was nearly independent of  $Re$ . In a more recent numerical analysis by Alghalibi *et al.* (2019), simulations of a spherical hyperelastic particle in a circular channel with  $d_0/D = 0.2$  were performed with  $100 \leq Re \leq 400$  and Weber number ( $We$ ) with  $0.125 \leq We \leq 4.0$ , the latter of which is the ratio of the inertial effect to the elastic effect acting on the particles. Their numerical results showed that regardless of  $Re$ , the final equilibrium position of a deformable particle is the centreline and harder particles (i.e. with lower  $We$ ) tended to rapidly migrate towards the channel centre (Alghalibi *et al.* 2019). The behaviour of a capsule subjected to pulsatile channel flow was addressed in the pioneering work by Maestre *et al.* (2019), where the migration velocity during axial focusing was investigated at  $O(Re) \leq 10^{-2}$  and  $d_0/D = 0.5$  for  $Ca = 0.075$ – $1.2$ . Despite these efforts, the inertial focusing of capsules subjected to pulsatile flow at finite inertia cannot be estimated based on these achievements.

Aiming for the precise description of the inertial focusing of spherical capsules in pulsatile channel flows, we thus perform numerical simulations of individual capsules with

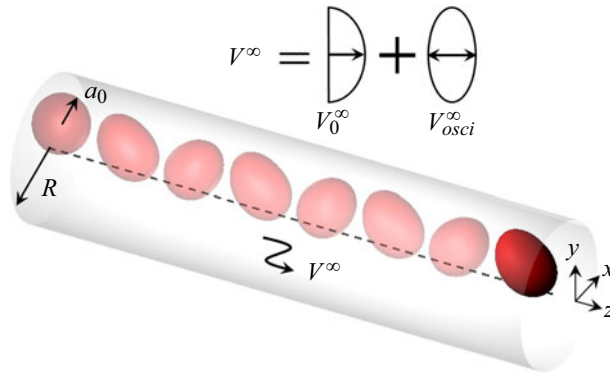


Figure 1. Visualisation of a spherical capsule with radius  $a_0$  in a channel with radius of  $R$  ( $R/a_0 = 2.5$ ) under a pulsatile flow with velocity  $V^\infty$ , which can be decomposed into the steady parabolic flow  $V_0^\infty$  and the oscillatory flow  $V_{osci}^\infty$  in the absence of any capsule. The capsule, initially placed at off-centre radial position  $r_{c0}^* = r_{c0}/R = 0.4$ , travels in the radial direction. In the figure, the lengths travelled by the capsule in the flow ( $z$ ) direction are not to scale for illustrative purpose. Hereafter, the same modification will be applied for visualisation.

a major diameter of  $d_0 = 2a_0 = 8 \mu\text{m}$  in a cylindrical microchannel with  $D = 2R = 20\text{--}50 \mu\text{m}$  (i.e.  $R/a_0 = 2.5\text{--}6.25$ ) for a wide range of oscillatory frequencies. Each capsule membrane, following the Skalak constitutive (SK) law (Skalak *et al.* 1973), is simulated for different  $Re$ ,  $Ca$  and size ratio  $R/a_0$ . Since this problem requires heavy computational resources, we resort to GPU computing, using the lattice-Boltzmann method (LBM) for the inner and outer fluids, and the finite-element method (FEM) to describe the deformation of the capsule membrane. This model has been successfully applied in the past for the analysis of the capsule flow in circular microchannels (Takeishi *et al.* 2022; Takeishi & Rosti 2023). The remainder of this paper is organised as follows. Section 2 gives the problem statement and numerical methods, and § 3 presents the numerical results for a single spherical capsule. Finally, a summary of the main conclusions is reported in § 4. A description of numerical verifications is presented in the Appendix.

## 2. Problem statement

### 2.1. Flow and capsule models and set-up

We consider the motion of an initially spherical capsule with diameter  $d_0$  ( $= 2a_0 = 8 \mu\text{m}$ ) flowing in a circular channel diameter  $D$  ( $= 2R = 20\text{--}50 \mu\text{m}$ ), with a resolution of 32 fluid lattices per capsule diameter  $d_0$ . The channel length is set to be  $20a_0$ , following a previous numerical study (Takeishi *et al.* 2022). Although we have investigated in the past the effect of the channel length  $L$  and the mesh resolutions on the trajectory of the capsule centroid (see figure 7 of Takeishi & Rosti 2023), we further assess the effect of this length on the lateral movement of a capsule in Appendix A (figure 12a).

The capsule consists of a Newtonian fluid enclosed by a thin elastic membrane, sketched in figure 1. The membrane is modelled as an isotropic and hyperelastic material following the SK law (Skalak *et al.* 1973), in which the strain energy  $w_{SK}$  and principal tensions in the membrane  $\tau_1$  and  $\tau_2$  (with  $\tau_1 \geq \tau_2$ ) are given by

$$\frac{w_{SK}}{G_s} = \frac{1}{4} \left( I_1^2 + 2I_1 - 2I_2 + CI_2^2 \right) \quad (2.1)$$

and

$$\frac{\tau_i}{G_s} = \frac{\eta_i}{\eta_j} \left[ \eta_i^2 - 1 + C \left( \eta_i^2 \eta_j^2 - 1 \right) \right] \quad \text{for } (i, j) = (1, 2) \text{ or } (2, 1). \quad (2.2)$$

Here,  $w_{SK}$  is the strain energy density function,  $G_s$  is the membrane shear elastic modulus,  $C$  is a coefficient representing the area incompressibility, and  $I_1 (= \eta_1^2 + \eta_2^2 - 2)$  and  $I_2 (= \eta_1^2 \eta_2^2 - 1)$  are the invariants of the strain tensor, with  $\eta_1$  and  $\eta_2$  being the principal extension ratios. In the SK law (2.1), the area dilation modulus is  $K_s = G_s(1 + 2C)$ . In this study, we set  $C = 10^2$  (Barthès-Biesel *et al.* 2002), which describes an almost incompressible membrane. Bending resistance is also considered (Li *et al.* 2005), with a bending modulus  $k_b = 5.0 \times 10^{-19}$  J (Puig-de-Morales-Marinkovic *et al.* 2007). These values have been shown to successfully reproduce the deformation of red blood cells in shear flow (Takeishi *et al.* 2014, 2019) and the thickness of the cell-depleted peripheral layer in circular channels (see figure A.1 of Takeishi *et al.* 2014). Neglecting inertial effects on the membrane deformation, the static local equilibrium equation of the membrane is given by

$$\nabla_s \cdot \boldsymbol{\tau} + \mathbf{q} = \mathbf{0}, \quad (2.3)$$

where  $\nabla_s (= (\mathbf{I} - \mathbf{nn}) \cdot \nabla)$  is the surface gradient operator,  $\mathbf{n}$  is the unit normal outward vector in the deformed state,  $\mathbf{q}$  is the load on the membrane and  $\boldsymbol{\tau}$  is the in-plane elastic tension that is obtained using the SK law (2.1).

The fluids are modelled with the incompressible Navier–Stokes equations for the fluid velocity  $\mathbf{v}$ :

$$\rho \left( \frac{\partial \mathbf{v}}{\partial t} + \mathbf{v} \cdot \nabla \mathbf{v} \right) = \nabla \cdot \boldsymbol{\sigma}^f + \rho \mathbf{f}, \quad (2.4)$$

$$\nabla \cdot \mathbf{v} = 0, \quad (2.5)$$

with

$$\boldsymbol{\sigma}^f = -p\mathbf{I} + \mu \left( \nabla \mathbf{v} + \nabla \mathbf{v}^T \right), \quad (2.6)$$

where  $\boldsymbol{\sigma}^f$  is the total stress tensor of the flow,  $p$  is the pressure,  $\rho$  is the fluid density,  $\mathbf{f}$  is the body force and  $\mu$  is the viscosity of the liquid, expressed using a volume fraction of the inner fluid  $\mathcal{I}$  ( $0 \leq \mathcal{I} \leq 1$ ) as

$$\mu = \{1 + (\lambda - 1)\mathcal{I}\} \mu_0, \quad (2.7)$$

where  $\lambda (= \mu_1/\mu_0)$  is the viscosity ratio,  $\mu_0$  is the external fluid viscosity and  $\mu_1$  is the internal fluid viscosity. No density contrast is considered; that is, the ratio of densities between the external and internal fluid is assumed to be one.

The dynamic condition coupling the different phases requires the load  $\mathbf{q}$  to be equal to the traction jump ( $\boldsymbol{\sigma}_{out}^f - \boldsymbol{\sigma}_{in}^f$ ) across the membrane:

$$\mathbf{q} = \left( \boldsymbol{\sigma}_{out}^f - \boldsymbol{\sigma}_{in}^f \right) \cdot \mathbf{n}, \quad (2.8)$$

where the subscripts ‘out’ and ‘in’ represent the outer and internal regions of the capsule, respectively.

The flow in the channel is sustained by a uniform pressure gradient  $\partial p_0/\partial z (= \partial_z p_0)$ , which can be related to the maximum fluid velocity in the channel by  $\partial_z p_0 = -4\mu_0 V_{max}^\infty/R^2$ . The pulsation is given by a superimposed sinusoidal function, such that the total pressure gradient is

$$\partial_z p(t) = \partial_z p_0 + \partial_z p_a \sin(2\pi ft). \quad (2.9)$$



The problem is governed by six main non-dimensional numbers, including: (i) the Reynolds number  $Re$  and (ii) the capillary number  $Ca$  defined as

$$Re = \frac{\rho D V_{max}^{\infty}}{\mu_0}, \quad (2.10)$$

$$Ca = \frac{\mu_0 \dot{\gamma}_m a_0}{G_s} = \frac{\mu_0 V_{max}^{\infty}}{G_s} \frac{a_0}{4R}, \quad (2.11)$$

where  $V_{max}^{\infty}$  ( $= 2V_m^{\infty}$ ) is the maximum fluid velocity in the absence of any cells,  $V_m^{\infty}$  is the mean fluid velocity and  $\dot{\gamma}_m$  ( $= V_m^{\infty}/D$ ) is the mean shear rate. Note that increasing  $Re$  under constant  $Ca$  corresponds to increasing  $G_s$ , namely, a harder capsule. Furthermore, we have: (iii) the viscosity ratio  $\lambda$ ; (iv) the size ratio  $R/a_0$ ; (v) the non-dimensional pulsation frequency  $f^* = f/\dot{\gamma}_m$  and (vi) the non-dimensional pulsation amplitude  $\partial_z p_a^* = \partial_z p_a / \partial_z p_0$ . Considering the focus of this study, we decided to primarily investigate the effect of  $Re$ ,  $R/a_0$  and  $f^*$ . Representative rigid and largely deformable capsules are considered with  $Ca = 0.05$  and  $Ca = 1.2$ , respectively.

When presenting the results, we will initially focus on the analysis of lateral movements of the capsule in effectively inertialess condition ( $Re = 0.2$ ) for  $R/a_0 = 2.5$ , and later consider variations of the size ratio  $R/a_0$ , viscosity ratio  $\lambda$ , Reynolds number  $Re$  ( $> 1$ ) and  $Ca$ . We confirmed that the flow at  $Re = 0.2$  well approximates an almost inertialess flow for single- (Takeishi & Rosti 2023) and multi-cellular flow (Takeishi *et al.* 2019). Unless otherwise specified, we show the results obtained with  $\partial_z p_a^* = 2$  and  $\lambda = 1$ .

## 2.2. Numerical simulation

The governing equations for the fluid are discretised by the LBM based on the D3Q19 model (Chen & Doolen 1998). We track the Lagrangian points of the membrane material points  $\mathbf{x}_m(\mathbf{X}_m, t)$  over time, where  $\mathbf{X}_m$  is a material point on the membrane in the reference state. Based on the virtual work principle, the above strong-form equation (2.3) can be rewritten in weak form as

$$\int_S \hat{\mathbf{u}} \cdot \mathbf{q} dS = \int_S \hat{\boldsymbol{\epsilon}} : \boldsymbol{\tau} dS, \quad (2.12)$$

where  $S$  is the surface area of the capsule membrane, and  $\hat{\mathbf{u}}$  and  $\hat{\boldsymbol{\epsilon}} = (\nabla_s \hat{\mathbf{u}} + \nabla_s \hat{\mathbf{u}}^T)/2$  are the virtual displacement and virtual strain, respectively. The FEM is used to solve (2.12) and obtain the load  $\mathbf{q}$  acting on the membrane (Walter *et al.* 2010). The velocity at the membrane node is obtained by interpolating the velocities at the fluid node using the immersed boundary method (Peskin 2002). The membrane node is updated by Lagrangian tracking with the no-slip condition. The explicit fourth-order Runge–Kutta method is used for the time integration. The volume-of-fluid method (Yokoi 2007) and front-tracking method (Unverdi & Tryggvason 1992) are employed to update the viscosity in the fluid lattices. A volume constraint is implemented to counteract the accumulation of small errors in the volume of the individual cells (Freund 2007): in our simulation, the relative volume error is always maintained lower than  $1.0 \times 10^{-3}$  %, as tested and validated in our previous study of cell flow in circular channels (Takeishi *et al.* 2016). All procedures were fully implemented on a GPU to accelerate the numerical simulation. More precise explanations for numerical simulations including membrane mechanics is provided in our previous works (see also Takeishi *et al.* 2019, 2022).

Periodic boundary conditions are imposed in the flow direction ( $z$ -direction). No-slip conditions are employed for the walls (radial direction). We set the mesh size of the LBM for the fluid solution to 250 nm and that of the finite elements describing the membrane to

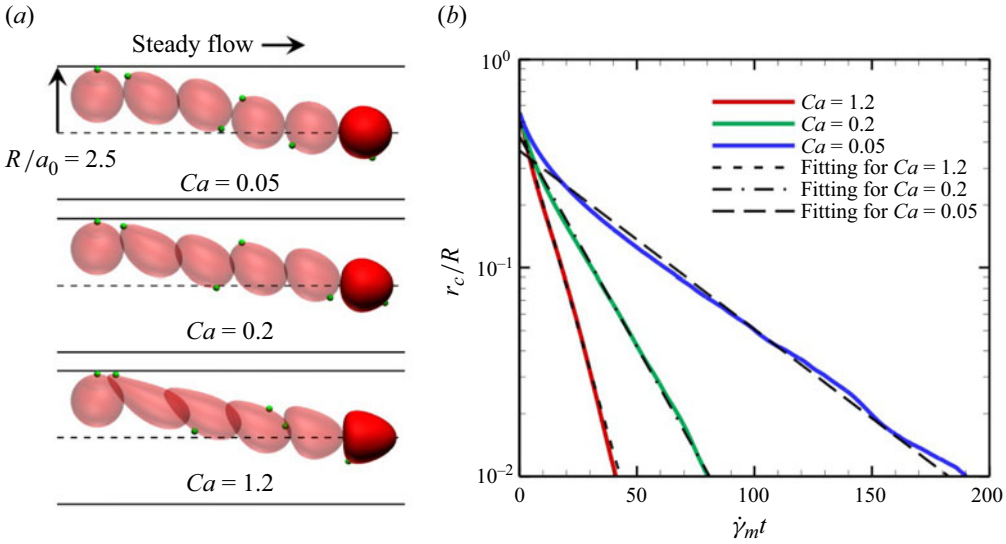


Figure 2. (a) Side views of the capsule during its axial focusing under steady flow for  $Ca = 0.05$  (top),  $Ca = 0.2$  (middle) and  $Ca = 1.2$  (bottom). The capsule is initially placed at  $r_{c0}^* = 0.55$ . The coloured dot on the membrane is shown to measure the membrane rotation. (b) Time histories of the radial position of these capsule centroids  $r_c/R$ . The dashed lines are the curves given by  $r_c^* = C_2 \exp(-C_1 t^*)$ , where  $r_c^*$  ( $= r_c/R$ ) is the non-dimensional capsule centroid,  $t^*$  ( $\dot{\gamma}_m t$ ) is the non-dimensional time, and  $C_1$  and  $C_2$  are the coefficients found by a least-squares fitting to the plot. The results in the figure are obtained for  $Re = 0.2$ ,  $R/a_0 = 2.5$  and  $\lambda = 1$ .

approximately 250 nm (an unstructured mesh with 5120 elements was used for the FEM). This resolution was shown to successfully represent single- and multi-cellular dynamics (Takeishi *et al.* 2019, 2022).

### 2.3. Analysis of capsule deformation

Later, we investigate the in-plane principal tension  $\tau_i$  (with  $\tau_1 \geq \tau_2$ ) and the isotropic tension  $\tau_{iso}$  in the membrane of the capsule. In the case of a two-dimensional isotropic elastic membrane, the isotropic membrane tension can be calculated by  $\tau_{iso} = (\tau_1 + \tau_2)/2$  for the deformed capsule. The averaged value of  $\tau_{iso}$  is then calculated as

$$\langle \tau_{iso} \rangle = \frac{1}{ST} \int_{\mathcal{T}} \int_S \tau_{iso}(\mathbf{x}_m, t) dS dt, \tag{2.13}$$

where  $\mathcal{T}$  is the period of the capsule motion. Hereafter,  $\langle \cdot \rangle$  denotes a spatial-temporal average. Time average starts after the trajectory has finished the initial transient dynamics, which differs for each case. For instance, at finite  $Re$  conditions, a quasi-steady state is usually attained around the non-dimensional time of  $\dot{\gamma}_m t = 200$ , and we start accumulating the statistics from  $\dot{\gamma}_m t \geq 400$  to fully cancel the influence of the initial conditions.

## 3. Results

### 3.1. Axial focusing of the capsule under steady channel flow ( $Re < 1$ )

We first investigate the axial focusing of a capsule under steady flow, which can be assumed to be effectively inertialess ( $Re = 0.2$ ). Figure 2(a) shows side views of the capsule during its axial focusing in the channel of size  $R/a_0 = 2.5$  for different  $Ca$  ( $= 0.05, 0.2$  and  $1.2$ ). The capsule, initially placed at  $r_{c0}^* = r_{c0}/R = 0.55$ , migrates after the flow onsets

Downloaded from https://www.cambridge.org/core. IP address: 3.15.226.150, on 17 Apr 2025 at 05:03:13, subject to the Cambridge Core terms of use, available at https://www.cambridge.org/core/terms. https://doi.org/10.1017/jfm.2025.184

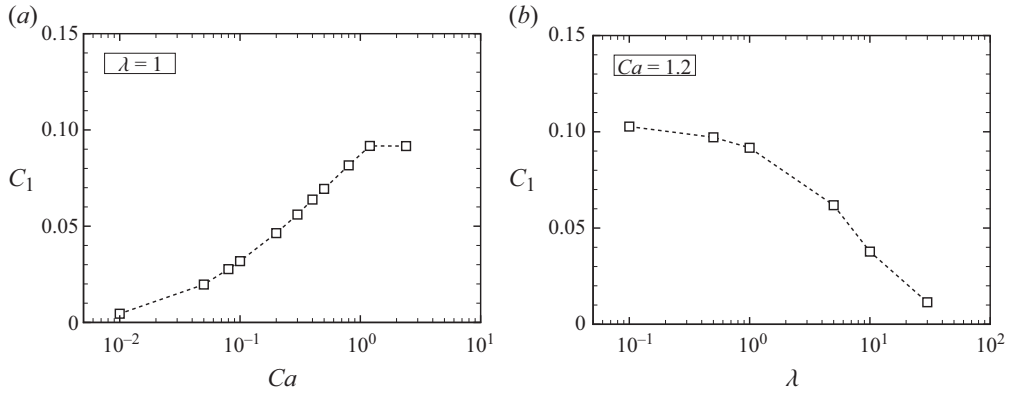


Figure 3. Coefficient  $C_1$  (a) as a function of  $Ca$  for  $\lambda = 1$  and (b) as a function of  $\lambda$  for  $Ca = 1.2$ . The results are obtained with  $Re = 0.2$ ,  $R/a_0 = 2.5$  and  $r_{c0}^* = 0.55$ .

towards the channel centreline (i.e. capsule centroid is  $r_c = 0$ ) while deforming, finally reaching its equilibrium position at the centreline where it achieves an axial-symmetric shape. Although the magnitude of deformation during axial focusing depends on  $Ca$ , these processes are commonly observed for every  $Ca$ . The time history of the radial position of the capsule centroid  $r_c$  is shown in figure 2(b). The results clearly show that the speed of axial focusing grows with  $Ca$ . Interestingly, all trajectories are well fitted by the following empirical expression:

$$r_c^* = C_2 \exp(-C_1 t^*), \tag{3.1}$$

where  $t^* (= \dot{\gamma}_m t)$  is the non-dimensional time, and  $C_1 (>0)$  and  $C_2$  are two coefficients that can be found by a least-squares fitting to the plot. Fittings are performed using data between the initial ( $r_{c0}^* = 0.55$ ) and final state ( $\Delta x_{LBM}/R \leq 0.01$  for  $R/a_0 = 2.5$ ), defined as the time when the capsule is within one mesh size ( $\Delta x_{LBM}$ ) from the channel axis.

Performing time differentiation of (3.1), the non-dimensional velocity of the capsule centroid  $\dot{r}_c^*$  can be estimated as

$$\dot{r}_c^* = -C_1 r_c^*. \tag{3.2}$$

This linear relation (3.2) may be understood by a shear-induced lift force proportional to the local shear strength. A more detailed description of the relationship between the coefficient  $C_1$  and the lift force on the capsule are provided in Appendix B.

Figure 3(a) shows the coefficient  $C_1$  as a function of  $Ca$ . As expected from figure 2(b), the value of  $C_1$  increases with  $Ca$ . Since the capsule deformability is also affected by the viscosity ratio  $\lambda$ , its influence on  $C_1$  is also investigated in figure 3(b). At a fixed  $Ca$  ( $= 1.2$ ), the value of  $C_1$  decreases with  $\lambda$ .

To further prove that  $C_1$  is independent of the initial radial position of the capsule centroid, additional numerical simulations are performed with a larger channel ( $R/a_0 = 5$ ) for different  $r_{c0}^*$ . Note that a case with larger channel for constant  $Re$  denotes smaller  $V_{max}^\infty$ , resulting in a smaller  $G_s$  (i.e. softer capsule) for constant  $Ca$ . Figure 4(a) is one of the additional runs at  $Ca = 0.2$ , where the capsule is initially placed at  $r_{c0}^* = 0.75$ . Figure 4(b) is the time history of the radial position of the capsule centroid  $r_c$  for different initial positions  $r_{c0}^*$ . We observe that the exponential fitting is still applicable for these runs, with the coefficient  $C_1$  reported in figure 4(c). These results provide a confirmation that  $C_1$  is indeed independent of the initial radial position  $r_{c0}^*$ . Furthermore, the fitting provided

Downloaded from https://www.cambridge.org/core. IP address: 3.15.226.150, on 17 Apr 2025 at 05:03:13, subject to the Cambridge Core terms of use, available at https://www.cambridge.org/core/terms. https://doi.org/10.1017/jfm.2025.184



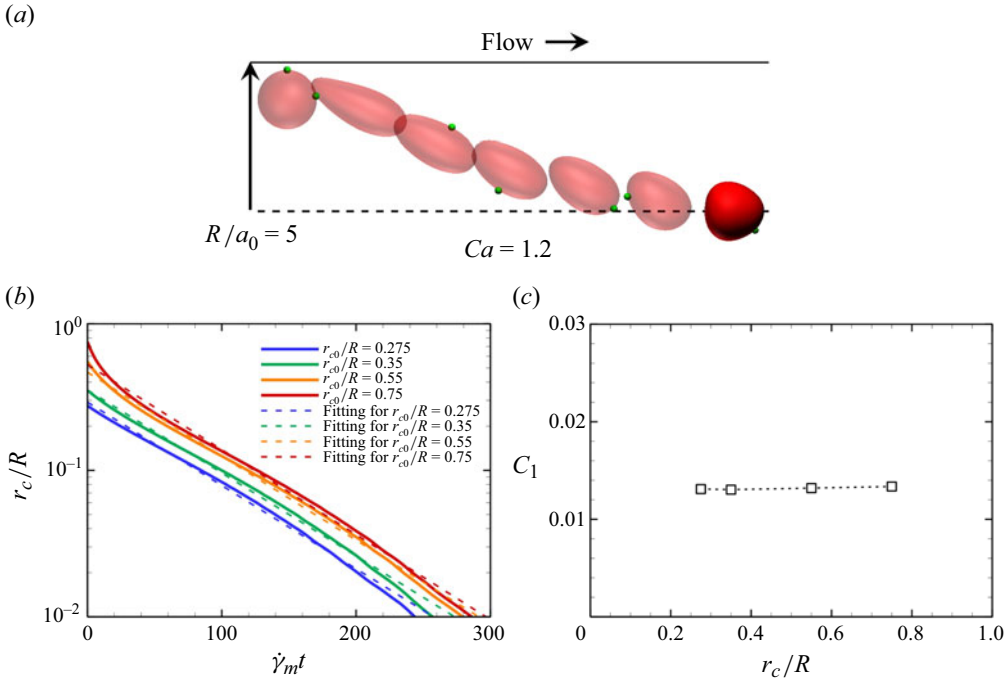


Figure 4. (a) Side views of a capsule with  $Ca = 1.2$  during its axial focusing for  $R/a_0 = 5$ , where the capsule is initially placed at  $r_{c0}^* = 0.75$ . (b) Time histories of the radial position of the capsule centroids  $r_c/R$  for different initial positions  $r_{c0}^*$ . (c) Coefficient  $C_1$  as a function of the initial position  $r_{c0}^*$ . The results are obtained with  $\lambda = 1$ .

in (3.1) is applicable even for a different constitutive law. Discussion of these results for capsule described by the neo-Hookean model, which features strain-softening, is reported in Appendix C (see also figure 13).

### 3.2. Capsule behaviour under pulsatile channel flow

Next, we investigate inertial focusing of capsules at finite  $Re$  and investigate whether the equilibrium radial position of the capsule can be altered by pulsations of the flow. Two representative behaviours of the capsule at low  $Ca$  ( $= 0.05$ ) and high  $Ca$  ( $= 1.2$ ) are shown in figure 5(a), which are obtained with  $f^* = 0.02$  and  $Re = 10$ . The simulations are started from an off-centre radial position  $r_{c0}^*$ . Hereafter, we consider the viscosity ratio  $\lambda = 1$  for simplicity. At the end of the migration, the least deformable capsule ( $Ca = 0.05$ ) exhibits an ellipsoidal shape with an off-centred position (figure 5a, left), while the most deformable one ( $Ca = 1.2$ ) exhibits the typical parachute shape at the channel centreline (figure 5a, right). Detailed trajectories of these capsule centroids  $r_c/R$  are shown in figure 5(b), where the non-dimensional oscillatory pressure gradient  $\partial_z p^*(t^*)$  ( $= 1 + 2 \sin(2\pi f^* t^*)$ ) is also displayed. The least deformable capsule ( $Ca = 0.05$ ) fluctuates around the off-centre position  $r_c/R$  ( $\approx 0.2$ ) and the waveform of  $r_c/R$  lags behind  $\partial_z p^*(t^*)$ . The capsule with large  $Ca$  ( $= 1.2$ ), however, immediately exhibits axial focusing, reaching the centreline within one flow period (figure 5b). Therefore, axial and off-centre focusing strongly depend on  $Ca$ .

Figure 5(c) is the time history of the isotropic tension  $\tau_{iso}$ . The major waveforms of  $\tau_{iso}$  are synchronised with  $\partial_z p^*$  in both  $Ca = 0.05$  and  $Ca = 1.2$ , thus indicating that

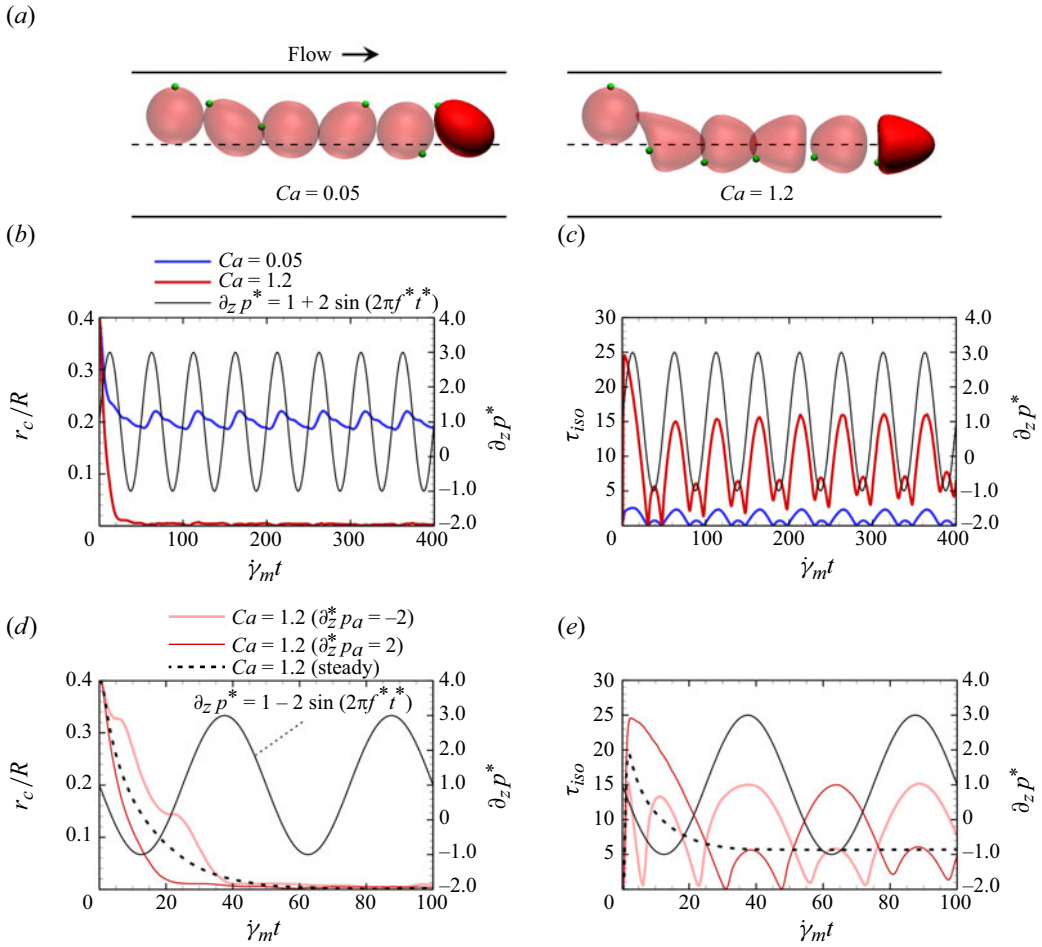


Figure 5. (a) Side views of the capsule during its migration at each time at  $f^* = 0.02$  for  $Ca = 0.05$  (left; see the supplementary movie 1, available at <https://doi.org/10.1017/jfm.2025.184>) and  $Ca = 1.2$  (right; see the supplementary movie 2). (b and c) Time histories of (b) the radial position of these capsule centroids  $r_c/R$  and (c) isotropic tensions  $\tau_{iso}$ , respectively. In panels (a)–(c), the results are obtained with  $\partial_z p_a^* = 2$ . (d and e) Time histories of (d)  $r_c/R$  and (e)  $\tau_{iso}$  for  $\partial_z p_a^* = -2$ , where those in steady flow are also superposed. In panels (b)–(e), non-dimensional pressure gradient  $\partial_z p^*$  is also displayed on the right axis. The results are obtained with  $Re = 10$ ,  $R/a_0 = 2.5$  and  $r_{c0}^* = 0.4$ .

the membrane tension spontaneously responds to the background fluid flow. The Taylor parameter, a classical index of deformation, is described in Appendix D (see figure 14).

To clarify whether fast axial focusing depends on the phase of oscillation or not, an antiphase pulsation (i.e.  $\partial_z p_a^* = -2$ ) is given by  $\partial_z p^*(t^*) = 1 - 2 \sin(2\pi f^* t^*)$ . Time histories of the capsule centroid  $r_c/R$  and membrane tension  $\tau_{iso}$  under such conditions are shown in figures 5(d) and 5(e), where the case at the same  $Ca = 1.2$  from figures 5(b) and 5(c) are also superposed for comparison, together with the solution for steady flow. Here, we define the focusing times  $T$  and  $T_{st}$  needed by the capsule centroid to reach the centreline (within a one fluid mesh corresponding to  $\sim 6\%$  of its radius to account for the oscillations in the capsule trajectory) under pulsatile and steady flows, respectively. Although the focusing time is decreased by almost 50% in prograde pulsation ( $\partial_z p_a^* = 2$ )

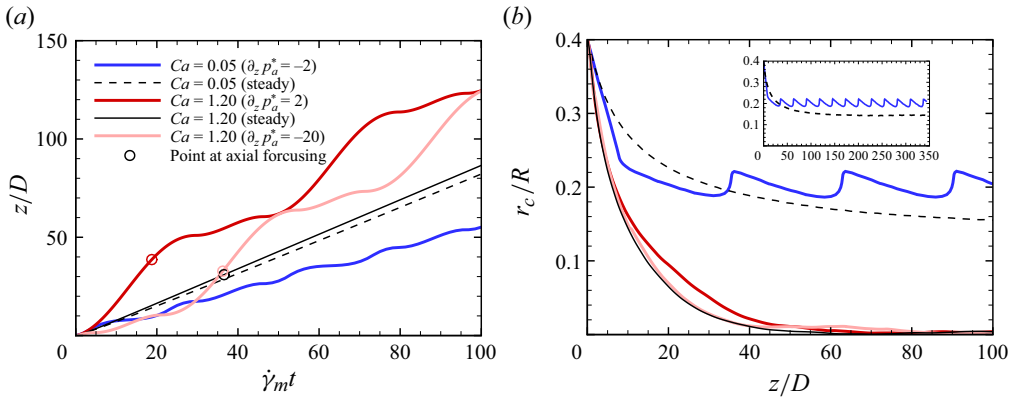


Figure 6. (a) Time history of the distance travelled along the flow direction ( $z$ -axis)  $z/D$  in the case shown in figure 5, where the circle dots represent the points when the capsule has completed the axial focusing. (b) Radial position of capsule centroids  $r_c/R$  as a function of  $z/D$ .

compared with that in the steady flow, the time in antiphase pulsation is decreased by only 1%. Such small acceleration in antiphase pulsation comes from relatively small deformation in early periods (figure 5e). We now understand that fast axial focusing relies on the large membrane tension after flow onset, and our numerical results exhibit the even faster axial focusing due to the pulsation of the flow.

Figure 6(a) is the time history of the distance travelled along the flow direction ( $z$ -axis)  $r_z/D$ . The distance to complete the axial focusing ( $Ca = 1.2$ ) under pulsatile flow increases compared with that in steady flow because the capsule speed along the flow direction increases by adding flow pulsation, where the circle dots represent the points when the capsule has completed the axial focusing. The capsule speed along the flow direction at  $Ca = 0.05$ , however, decreases with the pulsation of the flow. Figure 6(b) shows again the radial position of capsule centroids  $r_c/R$  as a function of  $z/D$ . The capsule trajectories obtained for  $Ca = 1.2$  remains almost the same, while the capsule trajectory for  $Ca = 0.05$  reaches equilibrium within a shorter travelled distance with pulsation. Following the classification by Vishwanathan & Juarez (2021), our problem is oscillatory dominated, since the oscillation amplitude is one order of magnitude greater than the steady flow component (i.e.  $O(s\omega/\bar{u}') \sim 10^1$ , where  $s$  is the centreline displacement amplitude and  $\bar{u}'$  is the centreline velocity in a steady flow component). Notwithstanding this, the oscillatory motion was not enough to enhance the inertial focusing, in terms of channel lengths needed for the inertial focusing, because of the capsule deformations impeding the inertial focusing, consistent with previous numerical study (see figure 4a of Takeishi *et al.* 2022).

We now focus on axial focusing (i.e. cases of relatively high  $Ca$ ) at finite  $Re$ . As discussed in figure 5(d), previous study showed that the speed of the axial focusing can be accelerated by the flow pulsation (Takeishi & Rosti 2023). An acceleration indicator of the axial focusing  $[1 - T/T_{st}]$  at  $Re = 10$  is summarised in figure 7, as a function of  $f^*$  ( $= f/\dot{\gamma}_m$ ), where the results at  $Re = 0.2$  (Takeishi & Rosti 2023) are also superposed. Although the initial radial position of the capsule  $r_{c0}^*$  is slightly different between the two  $Re$ , the focusing time is commonly minimised at a specific frequency in both cases. Note that the values of the dimensional frequency depend on the estimation of  $G_s$ , which varies with the membrane constitutive laws and which is also sensitive to different experimental methodologies, e.g. atomic force microscopy, micropipette aspiration, etc.

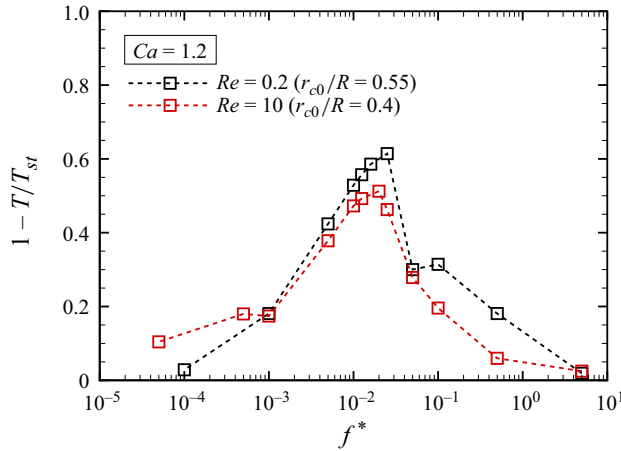


Figure 7. Acceleration indicator of the axial focusing  $[1 - T/T_{st}]$  as a function of the oscillatory frequency  $f^*$  for different  $Re$  ( $= 0.2$  and  $10$ ).  $T$  and  $T_{st}$  are the elapsed time needed by the capsule centroid to reach the centreline under pulsatile and steady flows, respectively. The initial radial position of the capsule is set to be  $r_{c0}^* = 0.55$  for  $Re = 0.2$  (see also figure 4a of Takeishi & Rosti 2023) and  $r_{c0}^* = 0.45$  for  $Re = 10$ . The results are obtained with  $Ca = 1.2$ .

(Bao & Suresh 2003); the estimation of the dimensional frequency is therefore not trivial. We hereby conclude that capsules with large  $Ca$  exhibit axial focusing even at finite  $Re$ , and that their equilibrium radial positions are not altered by the flow pulsation.

We speculate that the optimal focusing frequency of  $f^* \approx 0.02$ , corresponding to dimensional frequency of  $f = 20$  Hz, is the membrane resonance frequency, given a reference radius of  $a_0 = 4 \mu\text{m}$  and the surface shear elastic modulus of  $G_s = 4 \mu\text{N m}^{-1}$  (Takeishi *et al.* 2014). However, there is currently no clear theoretical framework on the resonance frequency of capsule. To provide further insights into the state of resonance, we constructed a 2-D fluid membrane model (or hydrodynamic equations of bilayer membrane), obtained by Onsager’s variation principle, wherein the fluid membrane is assumed to be an almost planar bilayer membrane (Takeishi *et al.* 2024c). Our numerical results showed that a membrane characteristic shift from an elastic-dominant to viscous-dominant state appears within the range  $40 \text{ Hz} \leq f \leq 400 \text{ Hz}$ , almost independently of surface tensions (figure 5c of Takeishi *et al.* 2024c). Since the resonance frequency can be formulated with intrinsic material (membrane) properties, it is expected that the value remains the same even under multi-capsule interactions. Indeed, we discovered that cross-over frequency of the storage and loss moduli in suspension of biconcave capsules modelling red blood cells (RBCs), whose inverse is defined as a relaxation time, is almost 40 Hz, regardless of the volume fraction of the capsules (figure 7f of Takeishi *et al.* 2024b). However note that the critical frequency was commonly estimated in terms of order of magnitude ( $O(f) = 10$  Hz) both in single- and multi-capsule dynamics as well as theoretical principles, since its exact estimation depends on  $G_s$ . Our recent numerical-experimental estimation strategy allows to quantify  $G_s$  of intact RBCs under dynamics and derive its value as  $\sim 0.5 \mu\text{N m}^{-1}$  (Takeishi *et al.* 2024a), which is one order of magnitude smaller than that obtained by the stretch test (Takeishi *et al.* 2014). Consequently, the dimensional optimal focusing frequency becomes  $O(f) = 10^2$  Hz, which is still in the range of the critical frequency estimated by the 2-D fluid membrane model (Takeishi *et al.* 2024c). These results form a fundamental basis for further studies on resonance frequency of plasma membrane.

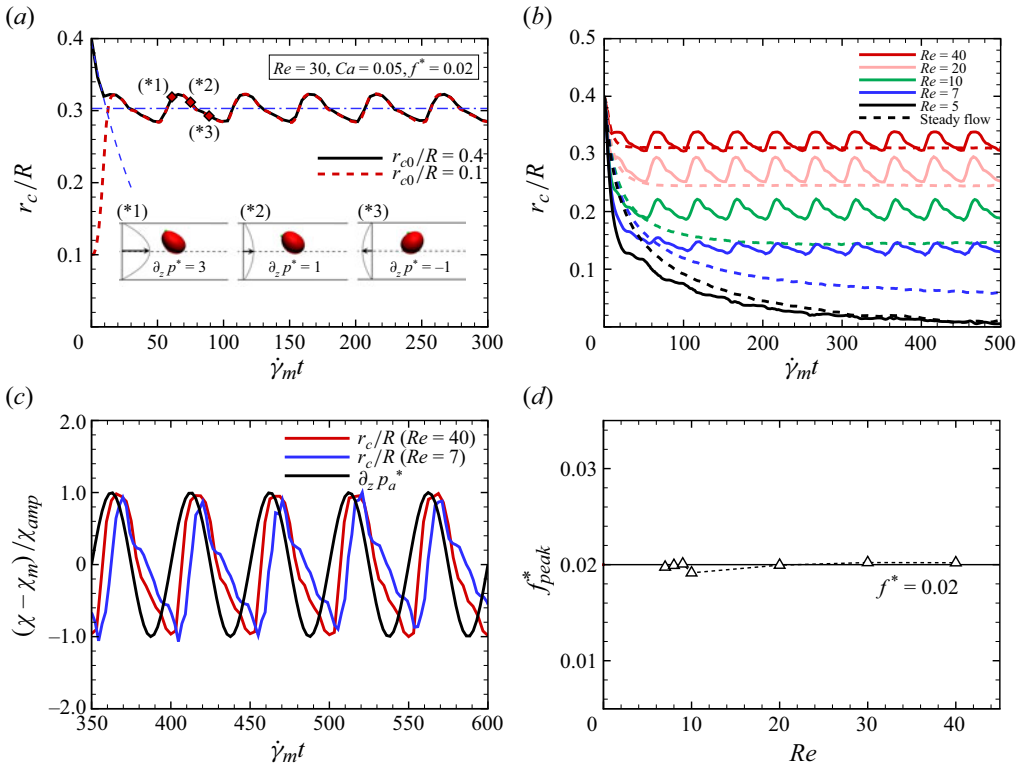


Figure 8. (a) Time histories of the radial position of the capsule centroid  $r_c/R$  at  $Re = 30$  and  $f^* = 0.02$  for different initial positions  $r_{c0}^*$  ( $= 0.1$  and  $0.4$ ), where insets represent snapshots of the lateral view of the deformed capsule at  $\dot{\gamma}_m t = (*1) 60, (*2) 75$  and  $(*3) 90$ . Dashed lines are the curves  $r_c^* = C_2 \exp(-C_1 t^*)$ , and the dash-dotted line denotes the equilibrium radial position of the capsule centroid. (b) Time histories of  $r_c/R$  for different  $Re$ , where dashed lines denote those in steady flow. (c) Time histories of  $r_c/R$  and  $\partial_z p_a^*$  at  $Re = 7$  (blue) and  $Re = 40$  (red), where the values are normalised by the amplitude  $\chi_{amp}$ , and are shifted so that each baseline is the corresponding mean value  $\chi_m$ . Data are shown after  $\dot{\gamma}_m t \geq 350$ . (d) Peak frequency  $f_{peak}^*$  of the capsule centroid  $r_c/R$ . The solid line in panel (c) denotes the oscillatory frequency  $f^* = 0.02$ . The results are obtained with  $Ca = 0.05$ ,  $R/a_0 = 2.5$  and  $r_{c0}^* = 0.4$ .

### 3.3. Effect of Reynolds number on capsule behaviour under pulsatile channel flow

We now focus on the inertial focusing of capsules at relatively small  $Ca$ , and, unless otherwise specified, we show the results obtained for  $Ca = 0.05$ . Figure 8(a) shows representative time history of the capsule centroid during inertial (or off-centre) focusing at  $Re = 30$  and  $f^* = 0.02$  for different initial position of the capsule  $r_{c0}^*$  ( $= 0.1$  and  $0.4$ ), where insets represent snapshots of the lateral view of the deformed capsule at various times  $\dot{\gamma}_m t$  ( $= 60, 75$  and  $90$ ), respectively. The results clearly show that the equilibrium radial position of the capsule is independent of its initial position  $r_{c0}$  (except when  $r_{c0} = 0$  for which the capsule remains at centreline). Hereafter, each run case is started from a slightly off-centre radial position  $r_{c0}^* = 0.4$  ( $R/a_0 = 2.5$ ). For the trajectory at early times ( $\dot{\gamma}_m t \leq 20$ ), fitting by (3.1) still works. At quasi-steady state ( $\dot{\gamma}_m t > 20$ ), the capsule centroid fluctuates around an off-centre position  $r_c/R$  ( $\approx 0.3$ ). Thus, the trajectory of the capsule during inertial focusing can be expressed as

$$r_c^* = \begin{cases} C_2 \exp(-C_1 t^*) & \text{for } t^* \leq t_{ax}^*, \\ r_e^* + \Delta r_{osci}^* & \text{for } t^* > t_{ax}^*, \end{cases} \quad (3.3)$$

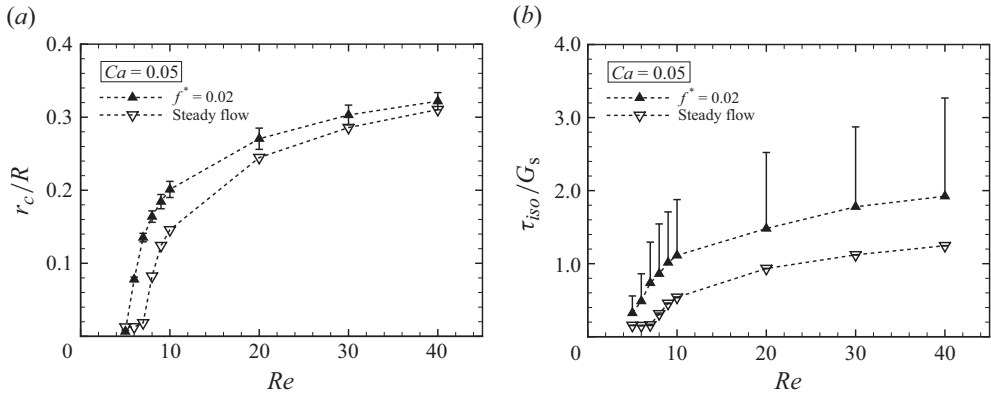


Figure 9. Time average of (a) the radial position of the capsule centroid  $\langle r_c \rangle / R$  and (b) isotropic tensions  $\langle \tau_{iso} \rangle$  as a function of  $Re$  at  $f^* = 0.02$ , where the error bars represent the standard deviation during a period. The error bars in panel (b) are displayed only on one side of the mean value for major clarity. The results are obtained with  $Ca = 0.05$ ,  $R/a_0 = 2.5$  and  $r_{c0}^* = 0.4$ .

where  $t_{ax}^*$  is the time period during axial focusing,  $r_e^*$  is the equilibrium radial position of the capsule centroid due to inertia and  $\Delta r_{osci}^*$  is a perturbation due to the oscillatory flow. Here, the equilibrium radial position is measured numerically by time averaging the radial position of the capsule centroid as  $r_e^* = \langle r_c^* \rangle = (1/T) \int_{t^*}^{t^*+T} r_c(t') dt'$ .

Figure 8(b) shows the time histories of the capsule centroid  $r_c/R$  at  $f^* = 0.02$  for different  $Re$ , together with those with steady flow. We observe that the radial positions are greater than those at steady flow for all  $Re$ , due to the larger values achieved by the pressure gradient during the pulsation. However, the actual contribution of the oscillatory flow to the inertial focusing depends on  $Re$ . For instance, for  $Re \leq 7$ , the capsule exhibits axial focusing at steady flow, but a pulsatile channel flow allows the capsule to exhibit off-centre focusing. Therefore, the pulsation itself can impede the axial focusing.

Figure 8(c) shows the waveforms of  $r_c/R$  at the end of the migration ( $\dot{\gamma}_m t \geq 350$ ), where the instantaneous values are normalised by their respective amplitudes  $\chi_{amp}$  and are shifted so that each baseline is the mean value  $\chi_m$ . Although the delay of  $r_c/R$  from the oscillatory pressure gradient  $\partial_z p^*$  tends to decrease as  $Re$  increases, the overall waveforms of  $r_c/R$  well follow that of  $\partial_z p^*$ , as shown in figure 5(b). To quantify the waveform of  $r_c/R$  and its correlation to  $\partial_z p^*$ , we extract the dominant (or peak) frequency  $f_{peak}^*$  of  $r_c/R$  with a discrete Fourier transform, whose principle and implementation are described by Takeishi *et al.* (2024b), and the result are shown as a function of  $Re$  in figures 8(d). In the cases of  $Re \leq 6$ , the capsule does not exhibit off-centre focusing and thus the plots are displayed for  $Re \geq 7$  only. The value of  $f_{peak}^*$  collapses on the frequency of  $\partial_z p^*$  with  $f^* = 0.02$  for  $Re \geq 7$  (figure 8d). The transition from the axial focusing to the off-centre focusing thus requires a synchronisation, induced by capsule deformability, between the capsule centroid and the background pressure gradient.

Figures 9(a) and 9(b) show the time average of the radial position or equilibrium position  $\langle r_c \rangle / R$  and the isotropic tension  $\langle \tau_{iso} \rangle$ , respectively, as a function of  $Re$ , where the error bars represent the standard deviation ( $SD$ ) during a period. Overall, both these values nonlinearly increase with  $Re$ , with the mean values in the oscillating flows always greater than those in steady flows. The curves show steep increases for  $Re \leq 10$ , followed by a more moderate increase for  $Re > 10$ ; these general tendencies are the same in steady or pulsatile flows. The effect of the flow pulsation is maximised at moderate  $Re$  ( $= 7$ ), in



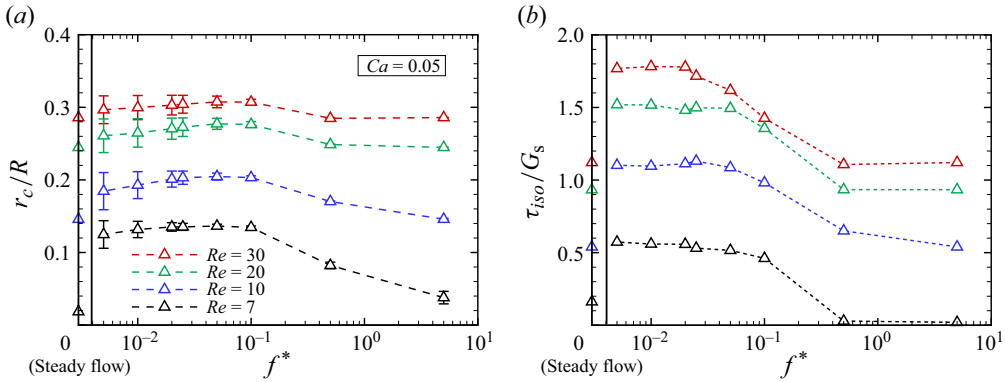


Figure 10. Time average of (a)  $\langle r_c \rangle / R$  and (b)  $\langle \tau_{iso} \rangle / R$  as a function of  $f^*$ . The error bars in panel (b) are not displayed to increase clarity. All results are obtained with  $R/a_0 = 2.5$ ,  $Re = 10$  and  $Ca = 0.05$ .

which the axial focusing is impeded by the pulsatile flow (figure 9a). The results also show that small fluctuations of the capsule radial position ( $SD(r_c/R) < 10^{-2}$ ) are accompanied by large fluctuations of the membrane tension ( $SD(\tau_{iso}) > 10^{-1}$ ).

### 3.4. Effect of oscillatory frequency on capsule behaviour under pulsatile channel flow

Finally, we investigate the effect of the oscillatory frequency  $f^*$  on the equilibrium radial position  $\langle r_c \rangle / R$  at  $Re = 10$ , with the results summarised in figure 10(a), where those at steady flow are also displayed at the point  $f^* = 0$ . The results clearly suggest that there exists a specific frequency to maximise  $\langle r_c \rangle / R$ , independent of  $Re$ . Interestingly, such an effective frequency ( $f^* = 0.05$ ) is close to or slightly larger than that maximising the axial focusing speed (see figure 7). Compared with steady flow, the equilibrium radial position  $\langle r_c \rangle / R$  at the effective frequency was enhanced by 640% at  $Re = 7$ , 40% at  $Re = 10$ , 13% at  $Re = 20$  and 7.6% at  $Re = 30$ . The contribution of the oscillatory flow to the off-centre focusing becomes negligible for higher frequencies, in which the trajectory of the capsule centroid at the highest frequency considered ( $f^* = 5$ ) collapses on that obtained with steady flow.

Figure 10(b) shows the time average of the isotropic tension  $\langle \tau_{iso} \rangle$  as a function of  $f^*$ . The values of  $\langle \tau_{iso} \rangle$  decrease as  $f^*$  increases because of the reduction of the shear stress when moving closer to the channel centreline (i.e. small  $\langle r_c \rangle / R$ ). The results of large capsule deformation at relatively small frequencies are consistent with a previous numerical study by Matsunaga *et al.* (2015), who showed that at high frequency, a neo-Hookean spherical capsule undergoing oscillating sinusoidal shear flow cannot adapt to the flow changes, and only slightly deforms, consistent with predictions obtained by asymptotic theory (Barthès-Biesel & Rallison 1981; Barthès-Biesel & Sgaier 1985). Thus, capsules at low frequencies exhibit an overshoot phenomenon, in which the peak deformation is larger than that its value in steady shear flow.

By increasing channel diameter  $D$  ( $= 2R = 30 \mu\text{m}$ ,  $40 \mu\text{m}$  and  $50 \mu\text{m}$ ), we also investigate the effect of the size ratio  $R/a_0$  ( $= 3.75$ ,  $5$  and  $6.25$ ) on the equilibrium radial position  $\langle r_c \rangle / R$ . Figure 11(a) is the time history of  $r_c/R$  for different size ratios  $R/a_0$  at  $Re = 30$  and  $f^* = 0.02$ , where the trajectories obtained with the steady flow are also displayed. All run cases are started from  $r_{c0}^* = 0.4$ . The equilibrium radial positions increase with  $R/a_0$ , while the contribution of oscillatory flow to  $\langle r_c \rangle / R$  becomes small as well as its fluctuation. This is quantified in figure 11(b), where  $\langle r_c \rangle / R$  is shown as a function of the size ratio  $R/a_0$ . Although the equilibrium radial position  $\langle r_c \rangle / R$  increases

Downloaded from https://www.cambridge.org/core. IP address: 3.15.226.150, on 17 Apr 2025 at 05:03:13, subject to the Cambridge Core terms of use, available at https://www.cambridge.org/core/terms. https://doi.org/10.1017/jfm.2025.184

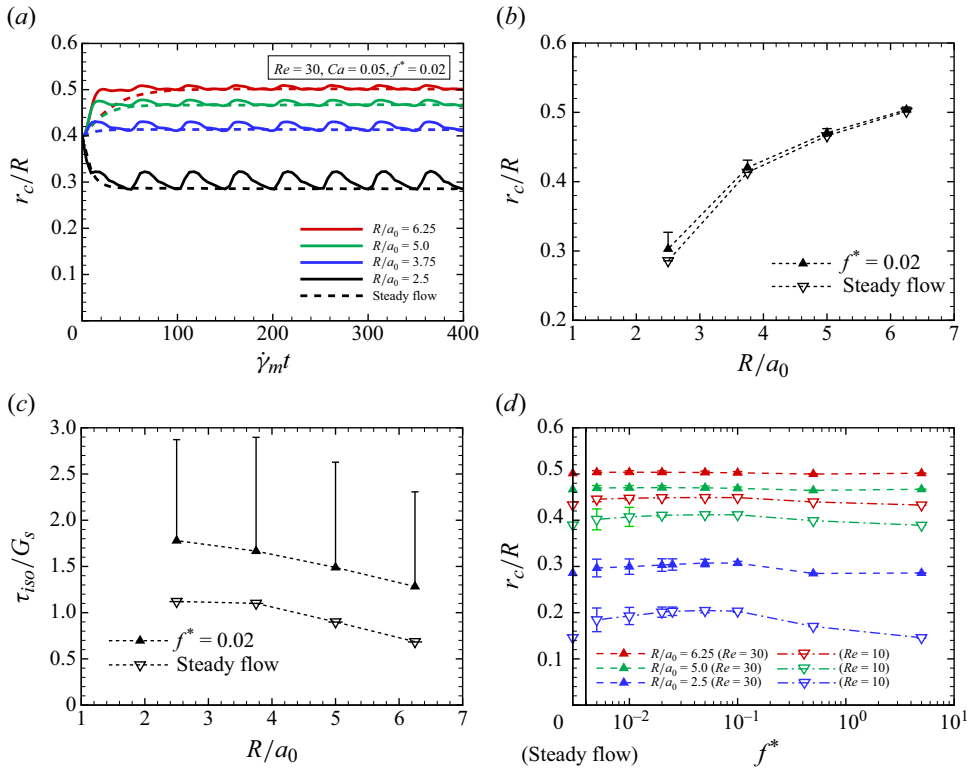


Figure 11. (a) Time history of  $r_c/R$  for different size ratios channel sizes  $R/a_0$ . (b and c) Time average of (b)  $\langle r_c \rangle / R$  and (c)  $\langle \tau_{iso} \rangle / G_s$  as a function of  $R/a_0$ . The error bars in panels (b) and (c) are displayed only on one side of the mean value for clarity. (d) Time average of  $\langle r_c \rangle / R$  at  $Ca = 0.05$  as a function of  $f^*$  for different  $R/a_0$ . All results are obtained with  $Re = 30, Ca = 0.05$  and  $f^* = 0.02$ , and data at  $Re = 10$  are superposed in panel (d).

with  $R/a_0$ , indicating that dimensional equilibrium radial position  $\langle r_c \rangle$  also increases with  $R$ , the isotropic tension  $\langle \tau_{iso} \rangle / G_s$  decreases, as shown in figure 11(c). This is because the distance from the capsule centroid to the wall ( $R - \langle r_c \rangle$ ) increases with  $R$ , resulting in lower shear stress. Oscillatory-dependent off-centre focusing is summarised in figure 11(d), where the results are obtained with different channel size  $R/a_0$  and different  $Re$  ( $= 10$  and  $30$ ). The result shows that oscillatory-dependent off-centre focusing is impeded as  $Re$  increases.

It is known that rigid particles align in an annulus at a radius of approximately  $0.6R$  for  $Re = D\bar{V}/\nu = O(1)$  (Segre & Silberberg 1962; Matas *et al.* 2004, 2009), and shift to larger radius for larger  $Re$  (Matas *et al.* 2004, 2009), where  $\bar{V}$  is the average axial velocity (Matas *et al.* 2004). Our numerical results show that capsules with low deformability ( $Ca = 0.05$ ) are still in  $\langle r_c \rangle / R \sim 0.5$  even for the largest channels ( $R/a_0 = 6.25; R = 25 \mu\text{m}$ ) and Reynolds number ( $Re = 30$ ), both in the steady and pulsatile flows (figure 11b). Therefore, off-centre focusing is impeded even at such small particle deformability. This result is consistent with previous numerical study about a spherical hyperelastic particle in a circular channel with  $R/a_0 = 5$  under steady flow for  $100 \leq Re \leq 400$  and  $0.00125 \leq We \leq 4$  (Alghalibi *et al.* 2019). There, the authors showed that the particle radial position is  $\langle r_c \rangle / R \sim 0.5$  at the highest  $Re$  ( $= 400$ ) and lowest  $We$  ( $= 0.00125$ ). Our numerical results further show that the contribution of the flow pulsation to the off-centre focusing

decreases as the channel size  $R/a_0$  increases (figures 11*b* and 11*d*) because of the low shear stress acting on the membranes (figure 11*c*). In other words, a large amplitude is required for oscillation-induced off-centre focusing in high- $Re$  and large channels.

The Poiseuille flow in a rigid circular pipe subject to the action of an oscillation pressure gradient was well described by Uchida (1956); Womersley (1955). At low frequency, oscillatory flow in the tube is better able to keep pace with the changing pressure. In the limit of zero frequency, the relation between flow and pressure is instantaneous as in a steady Poiseuille flow (see figure 16*a* in Appendix E). Thus, the particle (or capsule) is subject to shear stress, which results in its lateral movement due to the shear-induced lift force at low frequency. We confirmed it in figure 10(*a*), which is also consistent with the 2-D numerical results of a neutrally buoyant circular particle (Sun *et al.* 2009). However, since the mechanism of axial focusing of capsules is primarily attributed to their deformability, the frequency-dependent axial focusing of a rigid (circular) particle remains unclear. At high frequency, however, oscillatory flow in a channel is less able to keep pace with the changing pressure, thus reaching less than the fully developed Poiseuille flow profile (almost flat velocity profile) at the peak of each cycle (see figure 16*b* in Appendix E). In the limit of infinite frequency, the velocity reached at the peak of each cycle is zero, that is, the fluid does not move at all. Thus, the particle does not experience shear stress and maintains its lateral position at high frequency, consistent with the 2-D numerical analysis by Sun *et al.* (2009).

Furthermore, we showed that  $\langle r_c \rangle / R$  increased with  $Re (\leq 30)$ , results consistent with those of rigid spherical particles in three-dimensional (3-D) steady pipe flows (Sun *et al.* 2009). Such an increase in  $\langle r_c \rangle / R$  with  $Re$  can also be found for a rigid spherical particle on the square channel face, especially for  $Re \leq 100$  (Nakagawa *et al.* 2015), and also observed experimentally by Miura *et al.* (2014); Choi *et al.* (2011); Abbas *et al.* (2014). It is also known that the channel face equilibrium positions decrease with  $Re$ , in particular for  $Re > 100$ , while the channel corner equilibrium positions continue to increase with  $Re$  (Nakagawa *et al.* 2015). Although our numerical results described in figure 11(*d*) suggest that a large amplitude is required for oscillation-induced off-centre focusing at high  $Re$ , it remains an open question whether the off-centre focusing of capsules can indeed be enhanced by large-amplitude pulsatile flow and whether the optimal frequency remains consistent with the value measured in this study ( $f^* \approx 0.05$ ).

Throughout our analyses, we have quantified the radial position of the capsule in a tube based on the empirical expression (3.3). We have provided insights about the coefficient  $C_1 (> 0)$  in  $r_c^* = C_2 \exp(-C_1 t^*)$ , which potentially scales the lift force and depends on shape, i.e. capillary number  $Ca$  and viscosity ratio  $\lambda$ .

#### 4. Conclusion

We numerically investigated the lateral movement of spherical capsules in steady and pulsatile channel flows of a Newtonian fluid for a wide range of  $Re$  and oscillatory frequency  $f^*$ . The roles of size ratio  $R/a_0$ , and capillary number  $Ca$  on the lateral movement of the capsule have been evaluated and discussed. The first important question we focused on is whether a capsule lateral movement at finite  $Re$  in a pulsatile channel flow can be altered by its deformability. The second question is whether equilibrium radial positions or travelling time are controllable by oscillatory frequency.

Our numerical results showed that capsules with high  $Ca$  still exhibit axial focusing even at finite  $Re$  (e.g.  $Re = 10$ ) and that their equilibrium radial positions cannot be altered by flow pulsation. However, the speed of axial focusing at such high  $Ca$  is substantially accelerated by making the driving pressure gradient oscillating in time. We also confirmed

that there exists a most effective frequency ( $f^* \approx 0.02$ ), which maximises the speed of axial focusing, and that it remains the same as that in almost inertialess condition. For relatively low  $Ca$ , however, the capsule exhibits off-centre focusing, resulting in an equilibrium radial position  $\langle r_c \rangle / R$  that depends on  $Re$ . There also exists a specific frequency to maximise  $\langle r_c \rangle / R$ , which is independent of  $Re$ . Interestingly, such effective frequency ( $f^* \approx 0.05$ ) is close to that for axial focusing.

Frequency-dependent inertial focusing requires a synchronisation between the radial centroid position of the capsule and the background pressure gradient, resulting in periodic and large membrane tension, which impedes axial focusing. Such synchronisation abruptly appears at  $O(Re) = 10^0$  and shifts to an almost perfect synchronisation as  $Re$  increases. Thus, there is almost no contribution of flow pulsation to  $\langle r_c \rangle / R$  at relatively low  $Re$  ( $\leq 5$ ) or large  $Re$  ( $\geq 30$ ), while the contribution of the pulsation to  $\langle r_c \rangle / R$  is maximised at moderate  $Re$  ( $\approx 7$ ), allowing the capsule to exhibit axial focusing in steady flow. For constant amplitude of oscillatory pressure gradient, oscillatory-dependent inertial focusing is impeded as  $Re$  and the channel diameter increase, and thus a relatively large oscillatory amplitude is required in such high  $Re$  and large channels. Throughout our analyses, we have quantified the radial position of the capsule in a tube based on the empirical expression. We hereby conclude that the knowledge obtained under inertialess conditions (Takeishi & Rosti 2023) has been extended to cases involving finite  $Re$  ( $> 1$ ) conditions.

Given that the speed of inertial focusing can be controlled by oscillatory frequency, the results obtained here can be used for label-free cell alignment/sorting/separation techniques, e.g. for circulating tumour cells in cancer patients or precious haematopoietic cells such as colony-forming cells.

**Supplementary movies.** Supplementary movies are available at <https://doi.org/10.1017/jfm.2025.184>.

**Funding.** N.T. acknowledges funding from Daicel Corporation. K.I. acknowledges the Japan Society for the Promotion of Science (JSPS) KAKENHI for Transformative Research Areas A (Grant No. 21H05309) and the Japan Science and Technology Agency (JST), FOREST (Grant No. JPMJFR212N). This research was supported by the Okinawa Institute of Science and Technology Graduate University (OIST) with subsidy funding to M.E.R. from the Cabinet Office, Government of Japan. M.E.R. also acknowledges funding from the Japan Society for the Promotion of Science (JSPS), grants 24K17210 and 24K00810.

**Declaration of interests.** The authors report no conflict of interest.

## Appendix A. Numerical set-up and verification

To show that the channel length is adequate for studying the behaviour of a capsule that is subject to inertial flow, we have tested the channel length  $L$  ( $= 20a_0$  and  $40a_0$ ) and investigated its effect on the radial positions of the capsule centroids. The time history of the radial position of the capsule centroid  $r_c$  is compared among these different channel lengths in figure 12, where the centroid position  $r_c$  is normalised by the channel radius  $R$ . The results obtained with the channel length  $L$  used in the main work ( $= 20a_0$ ) are consistent with those obtained with twice longer channel ( $L = 40a_0$ ).

## Appendix B. Lift force on a capsule in a Poiseuille flow

We consider an object immersed in a Poiseuille flow, assuming that the flow is in the (steady) Stokes regime and that the object size is much smaller than the channel size. We also neglect any boundary effects acting on the object. Let  $y$  be the position relative to the channel centre. Due to the linearity of the Stokes equation, the object experiences a

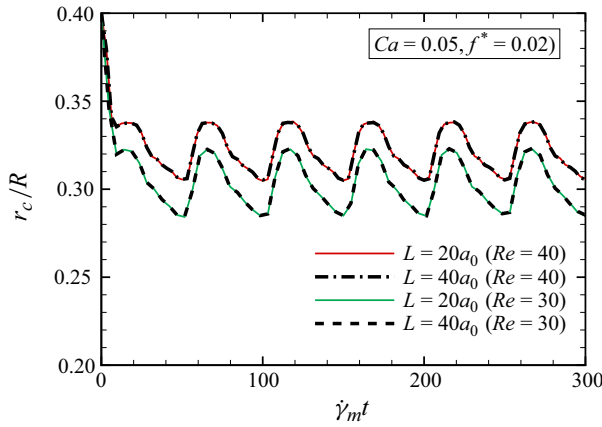


Figure 12. Time history of the radial position  $r/R$  for different channel lengths  $L$  ( $=20a_0$  and  $40a_0$ ) and different  $Re$  ( $=30$  and  $40$ ). In all runs, the capsule is initially placed at  $r_{c0}^* = 0.4$ . The results are obtained with  $R/a_0 = 2.5$  and  $Ca = 0.05$ .

hydrodynamic resistance proportional to its moving velocity, given by

$$f_1^L = -\xi_1 \dot{y}. \quad (\text{B1})$$

Note that the drag coefficient  $\xi_1 > 0$  is only determined by the viscosity and the shape (including the orientation) of the particle. We then consider the effects of the background Poiseuille flow. We have assumed that the channel size is much larger than the particle size, and hence the background flow to the particle is well approximated by a local shear flow with its local shear strength,

$$\dot{\gamma} = -2 \frac{V_{max}^\infty}{R^2} y. \quad (\text{B2})$$

In the presence of the background shear, the shear-induced lift force in general appears, and this is proportional to the shear strength (Kim & Karrila 2005),

$$f_2^L = -\xi_2 \dot{\gamma} = 2\xi_2 \frac{V_{max}^\infty}{R^2} y, \quad (\text{B3})$$

where the coefficient  $\xi_2$  is again only determined by the viscosity and the shape. The force balance equation on the  $y$ -direction therefore reads  $f_1^L + f_2^L = 0$ . If we introduce a new shape-dependent coefficient,  $C_1$ , as

$$C_1 = 2 \frac{\xi_2}{\xi_1} \frac{V_{max}^\infty}{R^2}, \quad (\text{B4})$$

we obtain the evolution equation for the position  $y$  as

$$\dot{y} = -C_1 y. \quad (\text{B5})$$

This equation is easily solved if  $C_1$  is constant and the result is the exponential accumulation to the channel centre, consistent with the numerical results.

### Appendix C. Neo-Hookean spherical capsule

In consideration of previous works by e.g. Lefebvre & Barthès-Biesel (2007) and Wang *et al.* (2021), the trajectory of capsule centroids are compared among different types of membrane constitutive laws for a comprehensive understanding of capsule motion in a

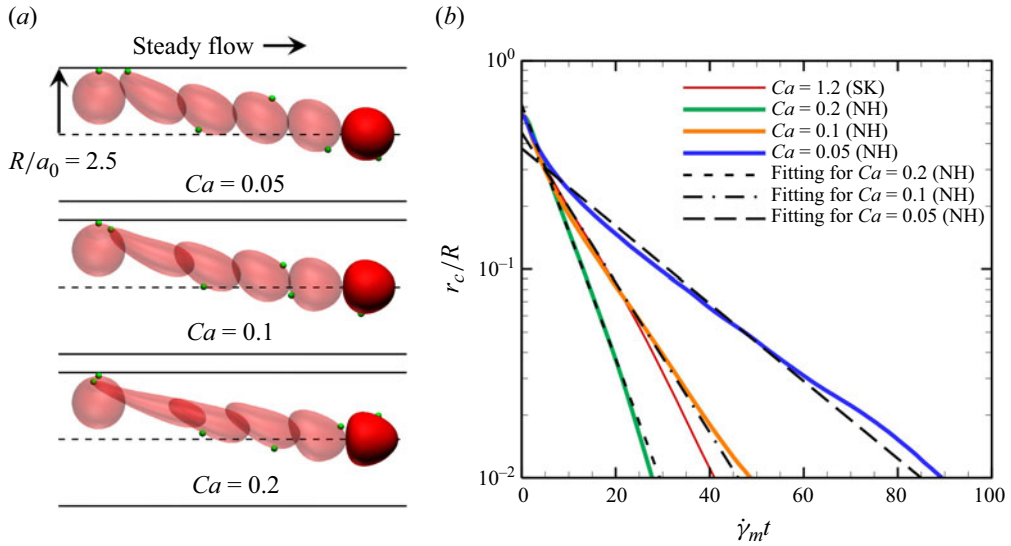


Figure 13. (a) Side views of the capsule during its axial focusing under steady flow for  $Ca = 0.05$  (top),  $Ca = 0.1$  (middle) and  $Ca = 0.2$  (bottom). The capsule is initially placed at  $r_{c0}^* = 0.55$ . (b) Time histories of the radial position of these capsule centroids  $r_c/R$ . The dashed lines are the curves  $r_c^* = C_2 \exp(-C_1 t^*)$ . The result at the highest  $Ca (= 1.2)$  obtained with SK law is also superposed. The results are obtained with  $Re = 0.2$ ,  $R/a_0 = 2.5$  and  $\lambda = 1$ .

tube and to verify whether our empirical expression (3.1) works independently of the membrane constitutive law. Here, let us take the NK constitutive law, which is given by

$$\frac{w_{NH}}{G_s} = \frac{1}{2} \left( I_1 - 1 + \frac{1}{I_2 + 1} \right). \quad (C1)$$

Figure 13(a) shows side views of the capsule during its axial focusing at each time for different  $Ca (= 0.05, 0.1 \text{ and } 0.2)$ . Other numerical settings ( $Re$ , initial position  $r_{c0}^*$  and viscosity ratio  $\lambda$ ) are the same as described in § 3.1. Even at relatively small  $Ca (= 0.2)$ , the neo-Hookean capsule exhibits large elongation after flow onsets, resulting in fast axial focusing. The trajectory and fitting for it at each  $Ca$  are shown in figure 13(b), where the result at the highest  $Ca (= 1.2)$  obtained with SK law described in figure 2(b) is also superposed. The results suggest that (3.1) still works even for neo-Hookean spherical capsules, although the applicable ranges of  $Ca$  are relatively small compared with those described by the SK law.

#### Appendix D. Taylor parameter

The SK spherical capsule deformation is quantified by the Taylor parameter  $D_{12}$ , defined as

$$D_{12} = \frac{|a_1 - a_2|}{a_1 + a_2}, \quad (D1)$$

where  $a_1$  and  $a_2$  are the lengths of the semi-major and semi-minor axes of the capsule, and are obtained from the eigenvalues of the inertia tensor of an equivalent ellipsoid approximating the deformed capsule (Ramanujan & Pozrikidis 1998).



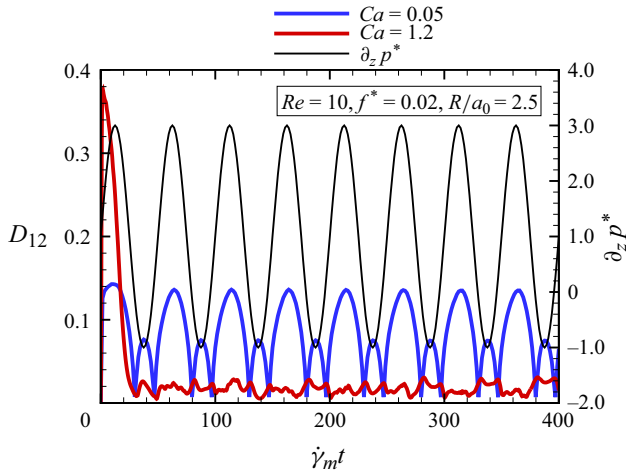


Figure 14. Time histories of the Taylor parameter  $D_{12}$  for different  $Ca$  ( $= 0.05$  and  $1.2$ ) at  $Re = 0.2$ . The results are obtained with  $f^* = 0.02$  and  $R/a_0 = 2.5$ .

Figure 14 shows the time history of  $D_{12}$  at  $Re = 10$ ,  $R/a_0 = 2.5$  and  $f^* = 0.02$ . Different from what is observed for the isotropic tension shown in figure 5(c), the off-centred capsule exhibits large  $D_{12}$ , which well responds to the oscillatory pressure  $\partial_z p^*$ . Thus, the magnitude of  $D_{12}$  is strongly correlated with the capsule radial position (and the consequent shear gradient).

Figure 15(a–c) shows the time average of  $D_{12}$ . Overall, these results exhibit trends comparable to those of  $\langle \tau_{iso} \rangle$ , previously shown in figures 9(b), 10(b) and 11(c). Despite the similarities, the axial-symmetric shaped capsule, typical of large  $Ca$ , exhibits small  $D_{12}$  (figure 15a), and the capsule membrane state in pipe flows cannot be easily estimated from the deformed shape. This is why we use the isotropic tension  $\tau_{iso}$  as an indicator of membrane deformation.

### Appendix E. Oscillatory velocity profile in a rigid tube

Let us consider the Poiseuille flow in a rigid tube, with the radius of  $R$ , subject to the action of an oscillation pressure gradient, as described by Uchida (1956); Womersley (1955). The governing equation for oscillatory flow in cylindrical coordinates  $(r, \theta, z)$  is

$$\frac{\partial^2 v_z}{\partial r^2} + \frac{1}{r} \frac{\partial v_z}{\partial r} - \frac{1}{v} \frac{\partial v_z}{\partial t} = \frac{1}{\mu} \frac{\partial p}{\partial z}, \quad (E1)$$

where the pressure gradient can be represented by a Fourier series

$$\frac{\partial p}{\partial z} = \sum_{k=0}^{\infty} c_k e^{ik\omega t}, \quad (E2)$$

with  $c_0$  corresponding to the time average pressure gradient producing the Poiseuille profile. The solution is sought in terms of the Fourier series

$$v_z(r, t) = \sum_{k=0}^{\infty} \hat{w}_k e^{ik\omega t}. \quad (E3)$$

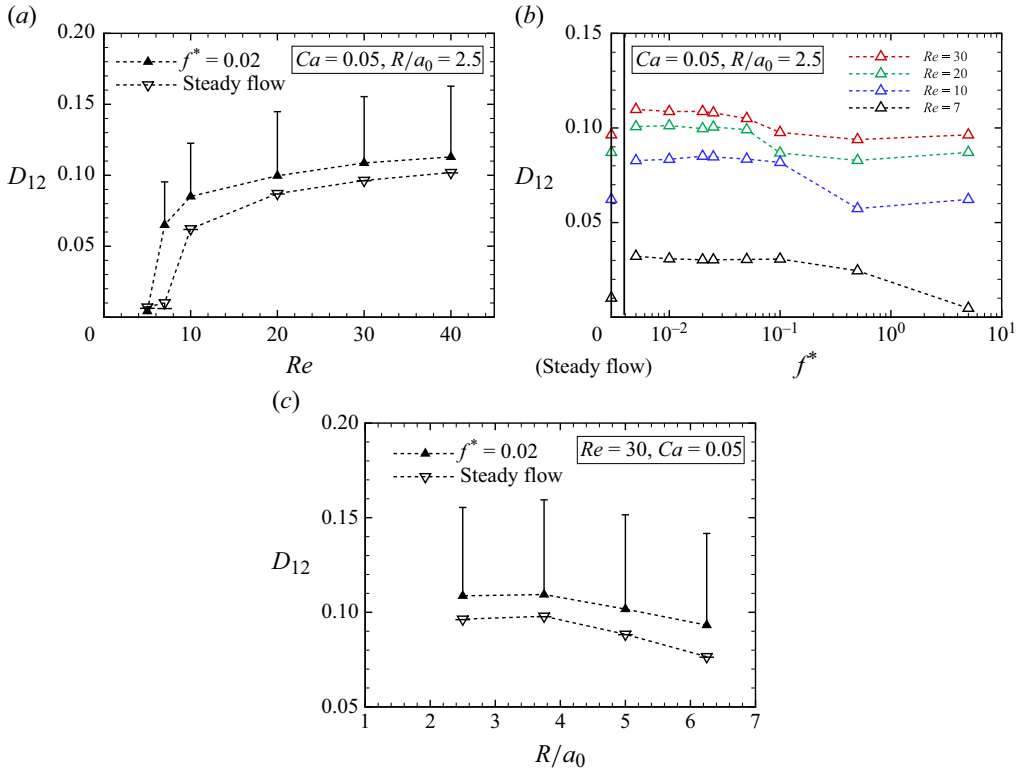


Figure 15. Time average of  $\langle D_{12} \rangle$  as a function of (a)  $Re$  (obtained with  $Ca = 0.05$  and  $R/a_0 = 2.5$ ), (b)  $f^*$  (obtained with  $Ca = 0.05$  and  $R/a_0 = 2.5$ ) and (c)  $R/a_0$  (obtained with  $Re = 10$  and  $Ca = 0.05$ ). The error bars in panels (a) and (c) are displayed only on one side of the mean value and are not displayed in panel (b) for clarity.

Inserting (E3) in (E1), one gets

$$\frac{d^2 \hat{w}_k}{dr^2} + \frac{1}{r} \frac{d\hat{w}_k}{dr} - \frac{i\omega k}{\nu} \hat{w}_k = \frac{c_k}{\mu}, \tag{E4}$$

where  $i^2 = -1$ , and defining the dimensionless variable  $\zeta = r/R$ , the non-homogeneous equation (E4) becomes

$$\frac{d^2 \hat{w}_k}{d\zeta^2} + \frac{1}{\zeta} \frac{d\hat{w}_k}{d\zeta} - ik\alpha^2 \hat{w}_k = \frac{c_k}{\mu}, \tag{E5}$$

where  $\alpha$  is the Womersley number,

$$\alpha = R \sqrt{\frac{\omega}{\nu}}. \tag{E6}$$

With the boundary conditions

$$\hat{w}_k|_{r=R} = 0, \quad \left. \frac{d\hat{w}_k}{dr} \right|_{r=0} = 0, \tag{E7}$$

the particular solution of (E5) is easily found to be  $-(i\omega k/\nu)\hat{w}_k = (c_k/\mu)$ , and thus the global solution of the equation (for  $k > 0$ ) is given by

$$\hat{w}_k = \frac{ic_k R^2}{\mu k \alpha^2} + C_1 J_0(\alpha \sqrt{k} \zeta i^{3/2}) + C_2 Y_0(\alpha \sqrt{k} \zeta i^{3/2}), \tag{E8}$$

where  $C_1, C_2$  are arbitrary constants, and  $J_0, Y_0$  are Bessel functions of order zero of the first and second kind, respectively. Recall that  $i^{1/2} = e^{i\pi/4} = (1+i)/\sqrt{2}$ .

The boundary conditions that the global solution must satisfy in a tube are the no-slip at the wall and the finite velocity along the axis of the tube, i.e.

$$\hat{w}_k(R) = 0, \quad |\hat{w}_k(0)| < \infty, \tag{E9}$$

which provide the required conditions to determine the constants  $C_1, C_2$ . It is known from the properties of  $Y_0(\zeta)$  that  $Y_0 \rightarrow \infty$  as  $\zeta$  (or  $r$ ) goes to 0. Thus, the second boundary condition in (E9) leads to  $C_2 = 0$ , and the first boundary condition then gives

$$C_1 = \frac{-ic_k R^2}{\mu \alpha_k^2 J_0(\alpha_k i^{3/2})}, \tag{E10}$$

where  $\alpha_k = \alpha \sqrt{k} = R \sqrt{k\omega/\nu}$ . With these values of  $C_1, C_2$ , the solution  $\hat{w}_k$  is finally

$$\hat{w}_k = \frac{ic_k R^2}{\mu \alpha_k^2} \left( 1 - \frac{J_0(\alpha_k \frac{r}{R} i^{3/2})}{J_0(\alpha_k i^{3/2})} \right) \tag{E11}$$

and the velocity profile  $v_z(r, t)$  is therefore

$$v_z(r, t) = -\frac{c_0 R^2}{4\mu} \left( 1 - \left(\frac{r}{R}\right)^2 \right) + \frac{R^2}{\mu} \sum_{k=1}^{\infty} \Re \left( \frac{ic_k}{\alpha_k^2} \left[ 1 - \frac{J_0(\alpha_k \frac{r}{R} i^{3/2})}{J_0(\alpha_k i^{3/2})} \right] e^{ik\omega t} \right), \tag{E12}$$

where  $\Re$  means the real part of a complex expression.

Let us consider oscillatory flow at low frequency, i.e. small  $\alpha$ . The Taylor series of  $J_0(\zeta i^{3/2})$  is

$$J_0(\zeta i^{3/2}) = 1 - \frac{(\zeta/2)^4}{(2!)^2} + \frac{(\zeta/2)^8}{(4!)^2} - \frac{(\zeta/2)^{12}}{(6!)^2} \dots + i \left( \frac{(\zeta/2)^4}{(1!)^2} + \frac{(\zeta/2)^6}{(3!)^2} - \frac{(\zeta/2)^{10}}{(5!)^2} - \dots \right), \tag{E13}$$

and taking the dominant terms into account, one obtains

$$\frac{J_0(\alpha_k \frac{r}{R} i^{3/2})}{J_0(\alpha_k i^{3/2})} = 1 - i \frac{\alpha_k^2}{4} \left( 1 - \left(\frac{r}{R}\right)^2 \right) - \frac{\alpha_k^4}{64} \left( 3 - 4 \left(\frac{r}{R}\right)^2 + \left(\frac{r}{R}\right)^4 \right) \sin \omega t + O(\alpha_k^6). \tag{E14}$$

The velocity is thus written as

$$v_z(r, t) = -\frac{c_0 R^2}{4\mu} \left( 1 - \left(\frac{r}{R}\right)^2 \right) - \frac{R^2}{\mu} \sum_{k=1}^{\infty} \left\{ \frac{c_k}{4} \left( 1 - \left(\frac{r}{R}\right)^2 \right) \cos(k\omega t) + \frac{c_k \alpha_k^2}{64} \left( 3 - 4 \left(\frac{r}{R}\right)^2 + \left(\frac{r}{R}\right)^4 \right) \sin(k\omega t) \right\}, \tag{E15}$$

Downloaded from https://www.cambridge.org/core. IP address: 3.15.226.150, on 17 Apr 2025 at 05:03:13, subject to the Cambridge Core terms of use, available at https://www.cambridge.org/core/terms. https://doi.org/10.1017/jfm.2025.184

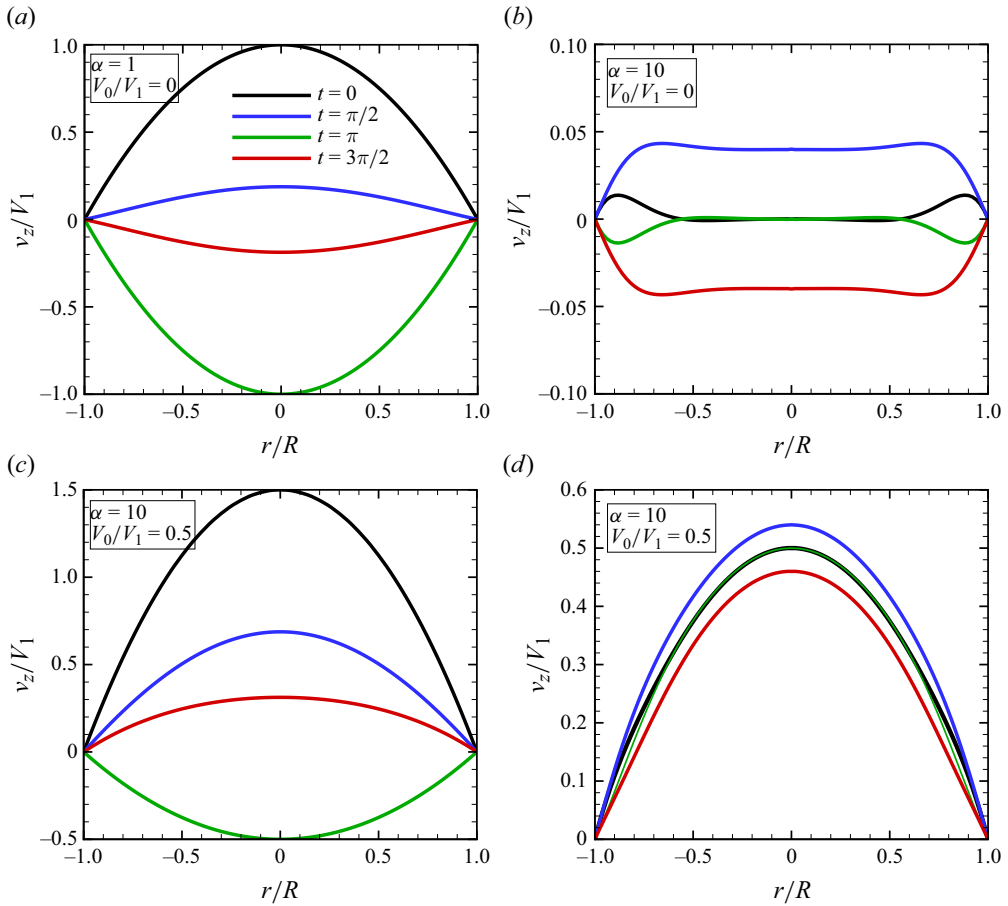


Figure 16. Oscillatory velocity profiles in a rigid tube at (a and c) low frequency ( $\alpha = 1$ ) and (b and d) high frequency ( $\alpha = 10$ ). The continuous Poiseuille component of the maximum velocity  $V_0$  is neglected in panels (a) and (b), while the finite value of  $V_0/V_1 = 0.5$ , which is the same condition used in the main text, is shown in panels (c) and (d). The lines represent the profiles at different phase angles ( $\omega t$ ) within the oscillatory cycle, starting from  $\omega t = 0$  and increasing by steps of  $\pi/2$ .

and if we set  $V_i = -(c_i R^2/4\mu)$  ( $i = 0, 1$ ) and  $\alpha_1 = \alpha$ , the first mode  $k = 1$  becomes

$$\frac{v_z}{V_1} = \frac{V_0}{V_1} \left( 1 - \left( \frac{r}{R} \right)^2 \right) + \left( 1 - \left( \frac{r}{R} \right)^2 \right) \cos(\omega t) + \frac{\alpha^2}{16} \left( 3 - 4 \left( \frac{r}{R} \right)^2 + \left( \frac{r}{R} \right)^4 \right) \sin(\omega t). \quad (\text{E17})$$

Figure 16(a) shows the velocity profile for  $\alpha = 1$  at each phase angle ( $= 0, \pi/2, \pi, 3\pi/4$ ) when the Poiseuille component of the velocity is neglected (i.e.  $V_0/V_1 = 0$ ). Starting from the Poiseuille flow at time  $\omega t = 0$ , at the phase of  $\omega t = \pi/2$ , the Poiseuille is still positive while the corresponding pressure gradient vanishes. The phase difference disappears at mid cycle ( $\omega t = \pi$ ) when the Poiseuille flow is recovered. The profile reaches its peak form at the peak pressure gradient ( $\omega t = 0, \pi$ ). The velocity profile for  $V_0/V_1 = 0.5$ , which is the same condition discussed in the main text, is also shown in figure 16(c) for completeness.

At high frequency, the oscillatory flow in a rigid tube is less able to keep pace with the changing pressure, thus reaching less than the fully developed Poiseuille flow profile at the peak of each cycle. The parameter  $\alpha r/R$  takes large values and the axis ( $r = 0$ ) is excluded

from the analysis. For high values of its argument, the asymptotic development of  $J_0(\zeta)$  is such that

$$J_0(\zeta) = \sqrt{\frac{2}{\pi\zeta}} \cos\left(\zeta - \frac{\pi}{4}\right) + O(|\zeta|^{-1}), \quad \text{with } |\arg(\zeta)| < 2\pi. \quad (\text{E18})$$

Using the relation  $i^{3/2} = e^{i3\pi/4}$  and  $s = \alpha_k r/R$ , we can perform the following algebraic calculation:

$$J_0(e^{i3\pi/4}s) = e^{-3\pi/8} \sqrt{\frac{2}{\pi s}} \cos\left(e^{i3\pi/4}s - \frac{\pi}{4}\right) \quad (\text{E19})$$

$$= e^{-i3\pi/8} \sqrt{\frac{2}{\pi s}} \cosh\left(\frac{s}{\sqrt{2}} + i\left(\frac{s}{\sqrt{2}} + \frac{\pi}{4}\right)\right), \quad (\text{E20})$$

and neglecting the decaying exponential in cosh, since we deal with large values of the argument, we obtain

$$J_0(e^{i3\pi/4}s) = e^{-3\pi/8} \frac{1}{\sqrt{2\pi s}} e^{\frac{s}{\sqrt{2}}} e^{i\left(\frac{s}{\sqrt{2}} + \frac{\pi}{4}\right)}, \quad (\text{E21})$$

which leads us to find

$$\frac{J_0(\alpha_k \frac{r}{R} i^{3/2})}{J_0(\alpha_k i^{3/2})} \approx \frac{1}{\sqrt{r/R}} e^{-(1+i)\frac{\alpha_k}{\sqrt{2}}(1-\frac{r}{R})}. \quad (\text{E22})$$

Finally, the first mode of the velocity profile yields

$$\begin{aligned} \frac{v_z}{V_1} = & \frac{V_0}{V_1} \left(1 - \left(\frac{r}{R}\right)^2\right) \\ & + \frac{4}{\alpha^2} \left[ \sin(\omega t) - \frac{1}{\sqrt{r/R}} e^{-\frac{\alpha}{\sqrt{2}}(1-\frac{r}{R})} \sin\left(\omega t - \frac{\alpha}{\sqrt{2}}\left(1 - \frac{r}{R}\right)\right) \right] + O\left(\frac{1}{\alpha^4}\right). \end{aligned} \quad (\text{E23})$$

Figure 16(b) shows the velocity profile for  $\alpha = 10$  at each phase angle, when the continuous Poiseuille component of the velocity is neglected. While the velocity is everywhere close to zero, the profile reaches its peak form at the phase of  $\omega t = \pi/2$  (and  $3\pi/2$ ), i.e. the resulting flow is in complete phase shift (by  $\pi/2$ ) with respect to the pressure gradient. The velocity profile for  $V_0/V_1 = 0.5$  is also shown in figure 16(d) for completeness. Thus, in this case, the continuous Poiseuille component is retained at each time.

#### REFERENCES

- ABBAS, M., MAGAUD, P., GAO, Y. & GEOFFROY, S. 2014 Migration of finite sized particles in a laminar square channel flow from low to high reynolds numbers. *Phys. Fluids* **26** (12), 123301.
- ALGHALIBI, D., ROSTI, M.E. & BRANDT, L. 2019 Inertial migration of a deformable particle in pipe flow. *Phys. Rev. Fluids* **4** (10), 104201.
- ASMOLOV, E.S. 1999 The inertial lift on a spherical particle in a plane Poiseuille flow at large channel Reynolds number. *J. Fluid Mech.* **381**, 63–87.
- BANERJEE, I., ROSTI, M.E., KUMAR, T., BRANDT, L. & RUSSOM, A. 2021 Analogue tuning of particle focusing in elasto-inertial flow. *Meccanica* **56** (7), 1739–1749.
- BAO, G. & SURESH, S. 2003 Cell and molecular mechanics of biological materials. *Nat. Mater.* **2** (11), 715–725.
- BARTHÈS-BIESEL, D., DIAZ, A. & DHENI, E. 2002 Effect of constitutive laws for two-dimensional membranes on flow-induced capsule deformation. *J. Fluid Mech.* **460**, 211–222.
- BARTHÈS-BIESEL, D. & RALLISON, J.M. 1981 The time-dependent deformation of a capsule freely suspended in a linear shear flow. *J. Fluid Mech.* **113**, 251–267.
- BARTHÈS-BIESEL, D. & SGAIER, H. 1985 Role of membrane viscosity in the orientation and deformation of a capsule suspended in shear flow. *J. Fluid Mech.* **160**, 119–135.

- BAZAZ, S.R., MASHHADIAN, A., EHSANI, A., SAHA, S.C., KRÜGER, T. & WARKIANI, M.E. 2020 Computational inertial microfluidics: a review. *Lab on a Chip* **20** (6), 1023–1048.
- CHEN, S. & DOOLEN, G.D. 1998 Lattice boltzmann method for fluid flow. *Annu. Rev. Fluid. Mech.* **30** (1), 329–364.
- CHEN, X., XUE, C., ZHANG, L., HU, G., JIANG, X. & SUN, J. 2014 Inertial migration of deformable droplets in a microchannel. *Phys. Fluids* **26** (11), 112003.
- CHOI, Y.-S., SEO, K.-W. & LEE, S.-J. 2011 Lateral and cross-lateral focusing of spherical particles in a square microchannel. *Lab on a Chip* **11** (3), 460–465.
- DI CARLO, D. 2009 Inertial microfluidics. *Lab on a Chip* **9** (21), 3038–3046.
- FENG, J., HU, H.H. & JOSEPH, D.D. 1994 Direct simulation of initial value problems for the motion of solid bodies in a Newtonian fluid. Part 2. Couette and Poiseuille flows. *J. Fluid Mech.* **277**, 271–301.
- FREUND, J.B. 2007 Leukocyte margination in a model microvessel. *Phys. Fluid* **19** (2), 023301.
- HADIKHANI, P., HASHEMI, S.M.H., BALESTRA, G., ZHU, L., MODESTINO, M.A., GALLAIRE, F. & PSALTIS, D. 2018 Inertial manipulation of bubbles in rectangular microfluidic channels. *Lab on a Chip* **18** (7), 1035–1046.
- HO, B.P. & LEAL, L.G. 1974 Inertial migration of rigid spheres in two-dimensional unidirectional flows. *J. Fluid Mech.* **65** (2), 365–400.
- HUR, S.C., HENDERSON-MACLENNAN, N.K., MCCABE, E.R.B. & DI CARLO, D. 2011 Deformability-based cell classification and enrichment using inertial microfluidics. *Lab on a Chip* **11** (5), 912–920.
- KARNIS, A., GOLDSMITH, H.L. & MASON, S.G. 1963 Axial migration of particles in Poiseuille flow. *Nature* **200** (4902), 159–160.
- KARNIS, A., GOLDSMITH, H.L. & MASON, S.G. 1966 The flow of suspensions through tubes: V. inertial effects. *Can. J. Chem. Engng* **44** (4), 181–193.
- KILIMNIK, A., MAO, W. & ALEXEEV, A. 2011 Inertial migration of deformable capsules in channel flow. *Phys. Fluids* **23** (12), 123302.
- KIM, S. & KARRILA, S.J. 2005 Microhydrodynamics—Principles and selected applications. In *Resistance and Mobility Relations. 5.2 The Resistance Tensor*, chap. 5, pp. 108–115. Dover Publications, Inc.
- LEFEBVRE, Y. & BARTHÈS-BIESEL, D. 2007 Motion of a capsule in a cylindrical tube: effect of membrane pre-stress. *J. Fluid Mech.* **589**, 157–181.
- LI, J., DAO, M., LIM, C.T. & SURESH, S. 2005 Spectrin-level modeling of the cytoskeleton and optical tweezers stretching of the erythrocyte. *Phys. Fluid* **88** (5), 3707–6719.
- MAESTRE, J., PALLARES, J., CUESTAA, I. & SCOTT, M.A. 2019 Dynamics of a capsule flowing in a tube under pulsatile flow. *J. Mech. Behav. Biomed. Mater.* **90**, 441–450.
- MARTEL, J.M. & TONER, M. 2014 Inertial focusing in microfluidics. *Annu. Rev. Biomed. Engng* **16** (1), 371–396.
- MATAS, J.P., MORRIS, J.F. & GUAZZELLI, E. 2009 Lateral force on a rigid sphere in large-inertia laminar pipe flow. *J. Fluid Mech.* **621**, 59–67.
- MATAS, J.-P., MORRIS, J.F. & GUAZZELLI, É. 2004 Inertial migration of rigid spherical particles in Poiseuille flow. *J. Fluid Mech.* **515**, 171–195.
- MATSUNAGA, D., IMAI, Y., YAMAGUCHI, T. & ISHIKAWA, T. 2015 Deformation of a spherical capsule under oscillating shear flow. *J. Fluid Mech.* **762**, 288–301.
- MIURA, K., ITANO, T. & SUGIHARA-SEKI, M. 2014 Inertial migration of neutrally buoyant spheres in a pressure-driven flow through square channels. *J. Fluid Mech.* **749**, 320–330.
- MUTLU, B.R., EDD, J.F. & TONER, M. 2018 Oscillatory inertial focusing in infinite microchannels. *Proc. Natl. Acad. Sci. USA* **115** (30), 7682–7687.
- NAKAGAWA, N., YABU, T., OTOMO, R., KASE, A., MAKINO, M., ITANO, T. & SUGIHARA-SEKI, M. 2015 Inertial migration of a spherical particle in laminar square channel flows from low to high Reynolds numbers. *J. Fluid Mech.* **779**, 776–793.
- PESKIN, C.S. 2002 The immersed boundary method. *Acta Numerica* **11**, 479–517.
- PUIG-DE-MORALES-MARINKOVIC, M., TURNER, K.T., BUTLER, J.P., FREDBERG, J.J. & SURESH, S. 2007 Viscoelasticity of the human red blood cell. *Am. J. Physiol. Cell Physiol.* **293** (2), C597–C605.
- RAFFIIE, A.H., DABIRI, S. & ARDEKANI, A.M. 2017 Elasto-inertial migration of deformable capsules in a microchannel. *Biomicrofluidics* **11** (6), 064113.
- RAMANUJAN, S. & POZRIKIDIS, C. 1998 Deformation of liquid capsules enclosed by elastic membranes in simple shear flow: large deformations and the effect of fluid viscosities. *J. Fluid Mech.* **361**, 117–143.
- SCHAAF, C. & STARK, H. 2017 Inertial migration and axial control of deformable capsules. *Soft Matter* **13** (19), 3544–3555.
- SCHONBERG, J.A. & HINCH, E.J. 1989 Inertial migration of a sphere in Poiseuille flow. *J. Fluid Mech.* **203**, 517–524.



- SEGRE, G. & SILBERBERG, A. 1962 Behaviour of macroscopic rigid spheres in Poiseuille flow Part 2. Experimental results and interpretation. *J. Fluid Mech.* **14** (1), 136–157.
- SHAO, X., YU, Z. & SUN, B. 2008 Inertial migration of spherical particles in circular Poiseuille flow at moderately high Reynolds numbers. *Phys. Fluids* **20** (10), 103307.
- SKALAK, R., TOZEREN, A., ZARDA, R.P. & CHIEN, S. 1973 Strain energy function of red blood cell membranes. *Biophys. J.* **13** (3), 245–264.
- SUN, B., YU, Z. & SHAO, X. 2009 Inertial migration of a circular particle in nonoscillatory and oscillatory pressure-driven flows at moderately high Reynolds numbers. *Fluid Dyn. Res.* **41** (5), 055501.
- TAKEISHI, N., IMAI, Y., ISHIDA, S., OMORI, T., KAMM, R.D. & ISHIKAWA, T. 2016 Cell adhesion during bullet motion in capillaries. *Am. J. Physiol. Heart Circ. Physiol.* **311** (2), H395–H403.
- TAKEISHI, N., IMAI, Y., NAKAOKI, K., YAMAGUCHI, T. & ISHIKAWA, T. 2014 Leukocyte margination at arteriole shear rate. *Physiol. Rep.* **2** (6), e12037.
- TAKEISHI, N., NISHIYAMA, T., NAGAISHI, K., NASHIMA, T. & SUGIHARA-SEKI, M. 2024a Numerical-experimental estimation of the deformability of human red blood cells from rheometrical data. *J. Rheol.* **68** (6), 837–848.
- TAKEISHI, N. & ROSTI, M.E. 2023 Enhanced axial migration of a deformable capsule in pulsatile channel flows. *Phys. Rev. Fluids* **8** (6), L061101.
- TAKEISHI, N., ROSTI, M.E., IMAI, Y., WADA, S. & BRANDT, L. 2019 Haemorheology in dilute, semi-dilute and dense suspensions of red blood cells. *J. Fluid Mech.* **872**, 818–848.
- TAKEISHI, N., ROSTI, M.E., YOKOYAMA, N. & BRANDT, L. 2024b Viscoelasticity of suspension of red blood cells under oscillatory shear flow. *Phys. Fluids* **36** (4), 041905.
- TAKEISHI, N., SANTO, M., YOKOYAMA, N. & WADA, S. 2024c Numerical analysis of viscoelasticity of two-dimensional fluid membranes under oscillatory loadings. *Results Engng* **22**, 102304.
- TAKEISHI, N., YAMASHITA, H., OMORI, T., YOKOYAMA, N., WADA, S. & SUGIHARA-SEKI, M. 2022 Inertial migration of red blood cells under a Newtonian fluid in a circular channel. *J. Fluid Mech.* **952**, A35.
- UCHIDA, S. 1956 The pulsating viscous flow superposed on the steady laminar motion of incompressible fluid in a circular pipe. *Z. Angew. Math. Phys.* **7** (5), 403–422.
- UNVERDI, S.O. & TRYGGVASON, G. 1992 A front-tracking method for viscous, incompressible, multi-fluid flows. *J. Comput. Phys.* **100** (1), 25–37.
- VISHWANATHAN, G. & JUAREZ, G. 2021 Inertial focusing in planar pulsatile flows. *J. Fluid Mech.* **921**, R1.
- WALTER, J., SALSAC, A.V., BARTHÈS-BIESEL, D. & LE TALLEC, P. 2010 Coupling of finite element and boundary integral methods for a capsule in a stokes flow. *Intl J. Numer. Meth. Engng* **83** (7), 829–850.
- WANG, X.-Y., MERLO, A., DUPONT, C., SALSAC, A.-V. & BARTHÈS-BIESEL, D. 2021 A microfluidic methodology to identify the mechanical properties of capsules: comparison with a microrheometric approach. *Flow* **1**, E8.
- WARKIANI, M.E., KHOO, B.L., WU, L., TAY, A.K.P., BHAGAT, A.A.S., HAN, J. & LIM, C.T. 2016 Ultrafast, label-free isolation of circulating tumor cells from blood using spiral microfluidics. *Nat. Protocols* **11** (1), 134–148.
- WOMERSLEY, J.R. 1955 Method for the calculation of velocity, rate flow, and viscous drag in arteries when the pressure gradient is known. *J. Physiol.* **127** (3), 553–563.
- YANG, B.H., WANG, J., JOSEPH, D.D., HU, H.H., PAN, T.-W. & GLOWINSKI, R. 2005 Migration of a sphere in tube flow. *J. Fluid Mech.* **540**, 109–131.
- YOKOI, K. 2007 Efficient implementation of THINC scheme: a simple and practical smoothed VOF algorithm. *J. Comput. Phys.* **226** (2), 1985–2002.
- YU, Z., PHAN-THIEN, N. & TANNER, R.I. 2004 Dynamic simulation of sphere motion in a vertical tube. *J. Fluid Mech.* **518**, 61–93.
- ZHOU, J., MUKHERJEE, P., GAO, H., LUAN, Q. & PAPAUTSKY, I. 2019 Label-free microfluidic sorting of microparticles. *APL Bioengng* **3** (4), 041504.